Laser Glazing of Rails
WBB/IWS Tests
(CNRC-Ottawa)

Saud Aldajah, George Fenske, and Layo Ajayi
(Energy Technology Division - ANL)

Claude Reed and Zach Xu
(Technology Development Division – ANL)

Ron DiMelfi
(Materials Research Development)

January 2005

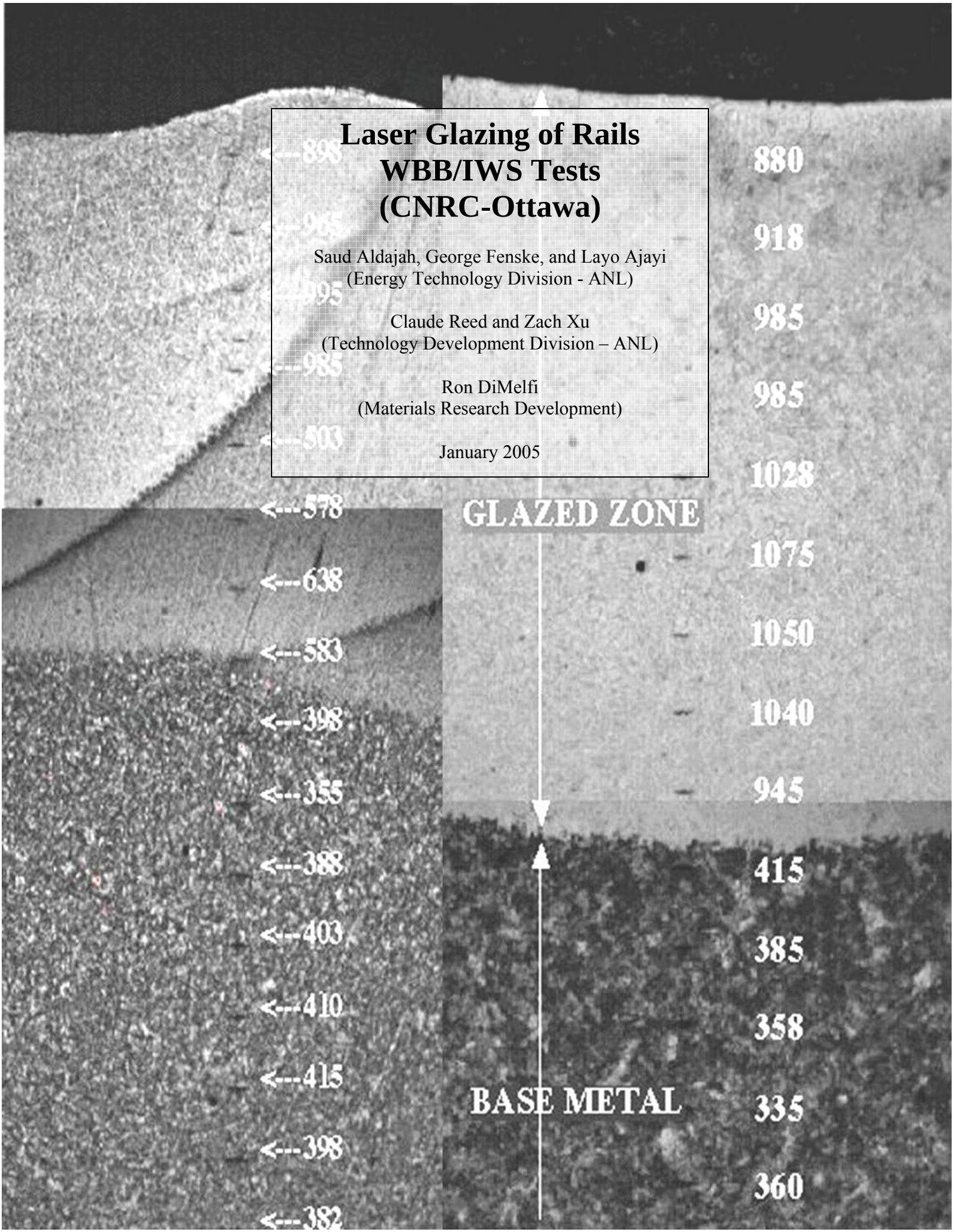

Abstract

Friction forces at wheel/rail interfaces are a significant parasitic energy loss that affects the efficiency with which goods are transported via rail. This report reviews the development of a laser glazing process that is designed to improve fuel efficiency b y treating the gauge face of rails to minimize wheel/rail forces. The research project (supported by the U.S. Department of Energy (DOE) Office of Energy Efficiency and Renewable Energy, FreedomCAR and Vehicle Technologies) involved activities to develop the laser glazing process, characterize the microstructure of glazed rail steel, assess friction forces with benchtop rigs, and perform full-scale friction force measurements with sets of full-scale instrumented railroad wheels.

The recent full-scale tests performed at the Canadian National Research Council Centre for Surface Transportation Technology in Ottawa, Ontario (hereafter referred to as "Ottawa tests") were performed with two objectives: first to confirm friction reduction observed in earlier (Association of American Railroads - AAR) rolling/sliding tests (and in subsequent lab-scale tests), and second to confirm the adhesion of a glazed layer to the underlying rail under typical loads (up to 38,000 lb). Demonstration of adhesion is critical not only for commercial acceptance of the process, but also for planning the next phase of research, which involves field tests of glazed rail segments.

The Ottawa tests confirmed the reduction in friction observed in prior rolling-sliding, tests performed at the AAR/Pueblo facility, and in benchtop tests, with friction reductions up to 40%. Evidence of cracking was observed, thus raising concerns about durability;

however, the extent and nature of the cracks were such that while they warrant further investigation, they should not preclude the field tests of glazed rail segments.

Introduction

Railroads are extremely important for the transportation of goods throughout the U.S., particularly for the transport of raw materials. In terms of ton-miles shipped, they are on equal par with trucks (Table 5.11 of Ref. 1), yet are much more efficient (Ref 1, Table 2.14), requiring only 1/10th the energy (346 Btu/ton-mile) when compared with trucks (3,337 Btu/ton-mile). Railroads consume approximately 4 billion gallons of diesel fuel each year to transport 1495 billion ton-miles of goods. This accounts for 2.3 % of all fuel used in 1997 in the U.S. at a cost of over $2 billion per year.

Because fuel costs are a significant portion of the total operating costs of transporting goods, fuel efficiency is an important factor in the design and operation of railroads. Several approaches are being considered to improve the efficiency of transporting goods by rail (Ref. 2). These approaches include efforts to improve

- the efficiency of diesel engines used to power locomotives (in-cylinder combustion and exhaust gas utilization),
- locomotive systems (idle reduction, energy recovery, and more efficient motors and drives),
- train systems (operations, consist, train fleet optimization and management, aerodynamic drag reduction, rolling resistance reduction, and reduction of wheel/rail friction)

The research described below addresses the concept of improving fuel economy by reducing wheel/rail friction, specifically, by reducing flange/rail friction. The sections below provide an overview of the impact of wheel/rail friction on train fuel consumption and the results that have been achieved with laser glazing at Argonne National Laboratory (ANL).

Past studies have indicated that energy savings could be as high as 24% when friction at the wheel/rail interface is properly managed. The key aspect is control of the friction forces. At the locomotive, high friction between the rail (specifically the top of the rail) and the wheel is desirable to ensure adequate traction to keep wheels from slipping and sliding when power is applied. Friction is also required under braking conditions to control the speed of downhill-bound trains or to bring a train to a safe stop. The trailing cars, however, require much lower friction levels under normal train operation. At these cars, a low, controllable friction is desirable and can significantly reduce the energy required to pull a train. Two regions account for most of the frictional losses between the wheel and the rail: the region between the top of the rail and the wheel tread, and the region between the wheel flange and the gauge face of the rail. Currently, wheel/rail lubrication (e.g., application of degradable greases and lubricants) is inconsistently applied and often disengaged by train crews. The research described herein focuses on the development of a laser glazing technique that imparts a durable, low-friction surface to the gauge face of the rails to reduce parasitic frictional losses between the flange and rail gauge.

Wheel/Rail Friction

A large portion of the energy consumed in rail transport is due to wheel/rail friction. The magnitude of the wheel/rail frictional energy losses relative to other energy loss mechanisms (e.g., aerodynamic drag, bearings, and grade) depends on the condition of the track (dry or wet), whether the track is tangential or curved, the truck design, wheel and rail profile, track wear, and train speed. Figures 1a and b (from Ref. 3) show the relative magnitudes of these forces for a 4700-ton train (consisting of 70 cars, half empty and half full, with an average weight of 70 tons) moving at 30 mph up a grade of 0.5% on dry and lubricated rail. Figure 1a shows the forces for movement along curved track, while 1b shows data for a tangential track. On curved track, flange/rolling resistance represents a significant fraction of the overall resistance, and a modest reduction (33%) in these forces will lead to a 13 % reduction in resistance (or fuel consumption). For tangent track, the flange contact contributes much less than curved track to overall resistance, and thus a modest reduction (33%) will lead to a smaller fuel savings (3% for the configuration analyzed for Fig. 1b). Nevertheless, 3 % is a significant improvement. At 4 billion gallons per year (roughly 250,000 barrels per day), a 3 % savings represents 120 million gallons per year (7500 barrels per day).

In addition to improved fuel efficiency, lower wheel/rail friction will have additional benefits, some of which indirectly affect fuel efficiency. Lower wheel/rail forces will reduce the tendency for "truck hunting" to occur. Typically, hunting occurs on tangential track with lightweight (empty) cars above 45 mph when cars oscillate between the tracks

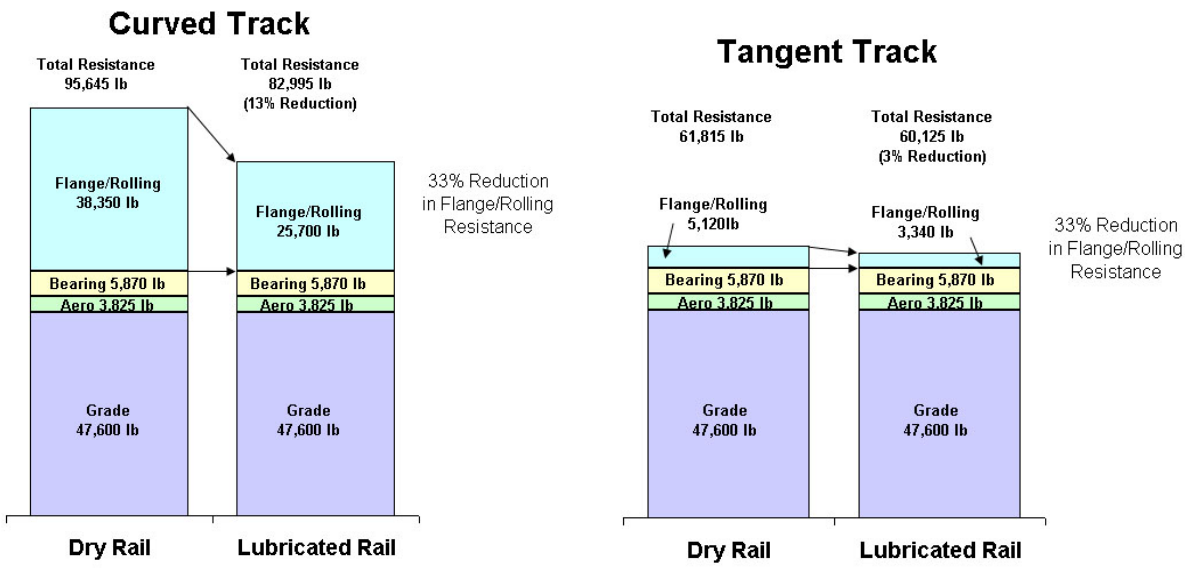

Figure 1. Train resistance components for curved and tangent track (Ref. 3)

and significantly increase energy use. Hunting also affects rail safety; if left unchecked, hunting can lead to derailment. Thus, reduction of wheel/rail forces will positively affect mitigation of hunting (and the potential for derailment). Alternatively, reduction of wheel/rail interface forces would enable trains to operate at higher speeds by minimizing the onset of hunting, and thereby improve productivity.

Laser Glazing

The objective of this project was to develop an advanced laser modification process to form a glaze on the gauge face of the rail. Initial results and models predicted the formation of a nanocrystalline surface layer that would impart low-friction properties at the interface. The project involved several tasks and included

- Process development (laser glazing),
- Friction and wear testing of laser-modified surfaces (glazed and shot-peened),

- Microstructural characterization of laser-modified surfaces,
- Development of a model (of surface deformation), and
- Full-scale friction testing of glazed rail.

Results (before Ottawa tests)

Process development. This effort primarily focused on laser glazing, a process that involves producing a thin molten layer on the surface, in contrast to laser hardening, in which no melting occurs. The project was initiated by Ron DiMelfi and much of the initial research and process development was performed by ANL's Laser Applications Laboratory (initially directed by Keng Leong, later, by Claude Reed and Zach Xu). The most recent laser glazing activities (in preparation for the Ottawa tests) were performed by NuVonyx (Ref 4). Initial glazing activities at ANL involved parametric studies to optimize the conditions under which a glazed layer forms on 1080 steel when an Electrox 1.6-kW pulsed Nd:YAG laser with fiber-optic beam delivery and special beam shaping optics. In the early studies, two approaches were developed: one that involved a single pass of the laser over a given area, and one that involved multiple overlapping passes (Fig. 2). The Knoop hardness of the martensitic glazed regions was 2-3 times greater than that of the substrate, depending on whether a single-pass (factor of 3 times harder) or multipass (slightly over 2 times harder) process was used.

The initial ANL efforts were performed at relatively slow glazing speeds (5 mm/s) and produced rough surfaces (see Fig. 3a). Later attempts to operate at higher glazing speeds (10 mm/s) produced smoother surfaces (Fig. 3b). A commercial laser glazing process

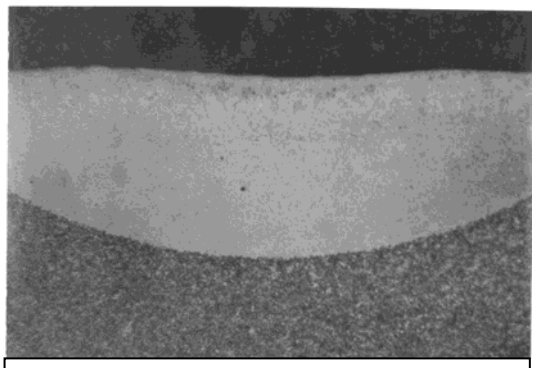

Figure 2a: Single pass laser glazed cross section.

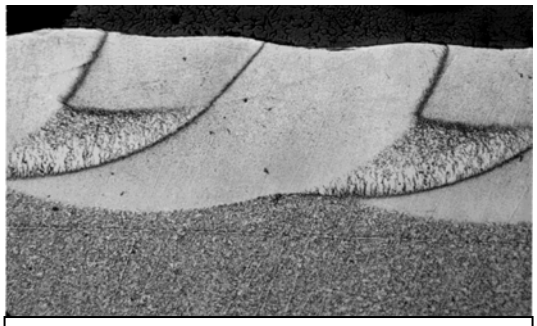

Figure 2b. Multi pass laser-glazed cross section

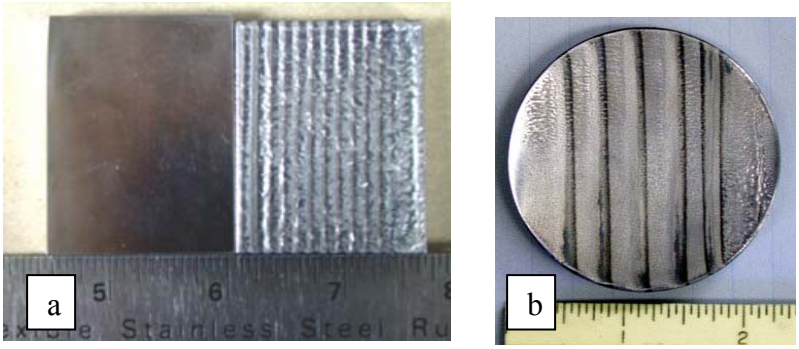

Figure 3. Glazed steel: (a) 5 mm/s, and (b) 10 mm/s

that utilized high-power diode laser technology was also investigated. In this case, bars of 1080 steel were processed by a commercial vendor (NuVonyx - http://www.nuvonyx.com/) and subsequently tested at ANL (Fig. 4a). A third modification of the process (laser shot-peening [LSP]) was also evaluated. Bars of 1080 steel were processed by LSPT (LSP Technologies - http://www.lspt.com/home.asp) to 'peen' near-surface regions (Fig. 4b). LSP does not involve melting near-surface regions; instead, it utilizes a laser to shock near-surface regions, thereby introducing high compressive stresses and increasing hardness.

Friction and wear. Tests of friction and wear were performed on laser-treated coupons (primarily ANL-glazed steels) to evaluate the potential of glazing to reduce frictional

Figure 4a. 1080 steel glazed with high-power diode laser

Figure 4b. 1080 steel laser peened (right side) and glazed and peened (left side)

losses between the wheel flange and the gauge face of the rail. Initial tests (Ref. 5) were performed at Falex Corporation in a low-speed block-on-ring configuration, and at the (AAR) test facility in Pueblo, CO with a full-scale ring/wheel-on-block/rail, operated under controlled slip conditions. Detailed tests were performed at ANL on twin-roller, pin-on-disc (POD), and reciprocating pin-on-flat configurations.

The block-on-ring tests at Falex measured the breakaway (e.g., static friction coefficient) torque/force required to initiate rotation (defined as 0.013 rpm) under various loads (445-4005 N [100-900 lb]) in 100-lb (445-N) increments. (The ring in this case was a Falex standard ring, 'S-10 steel' with a Rc of 58-63; the block was 1080 rail steel, as-received or glazed.) Dynamic block-on-ring tests were not performed because earlier tests showed that debris accumulation produced unreliable comparisons under dry, heavily loaded conditions. The Falex test results showed static friction coefficients for untreated 1080 of ≈ 0.35-0.45, which dropped to values that ranged from 0.2 to 0.4 for differing glazing conditions.

The AAR tests were similar to the Falex tests in that they measured the breakaway friction (friction to start rotation) and the friction during maintained rotation, but on a much larger scale. The AAR tests were performed on a segment of rail that was glazed on the top of the rail; the top of the rail was subjected to pure rolling and, at the end, to rolling/sliding contact (Fig. 5). The static friction coefficient of the untreated 1080 rail varied from 0.2 to 0.5, depending on the applied load, whereas the friction coefficient of the glazed regions varied from 0.1 to 0.25. Dynamic friction coefficients for the glazed regions varied from 0.2 to 0.35, depending on load, compared to 0.2 to 0.55 for unglazed regions.

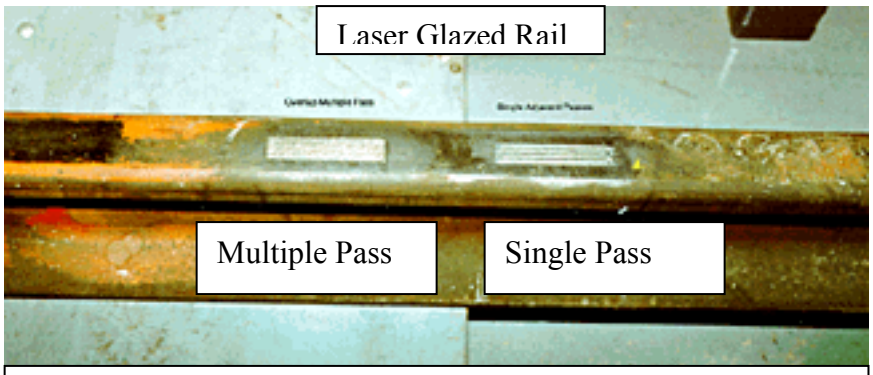

Figure 5. Segment of laser-glazed 1080 rail used in AAR friction tests

The benchtop tests at ANL were more controlled than the full-scale tests at the AAR facilities. The environment was more repeatable in terms of surface contaminants and more consistent in terms of relative humidity, two factors that significantly affect the frictional response. The POD tests used flats of 1080 steel, glazed and unglazed, that rubbed against stationary balls or pins (52100, 1080 steel, 440C, or alumina). The tests revealed that the composition of the pin/ball significantly affected the friction coefficient

(Fig. 6). The general trend was that the glazing reduced the friction coefficient by 3-35%, depending on the material. The greatest reduction was for an alumina ball sliding against the 1080 steel, suggesting that a strong chemical adhesion mechanism may be active with the metallic counterparts.

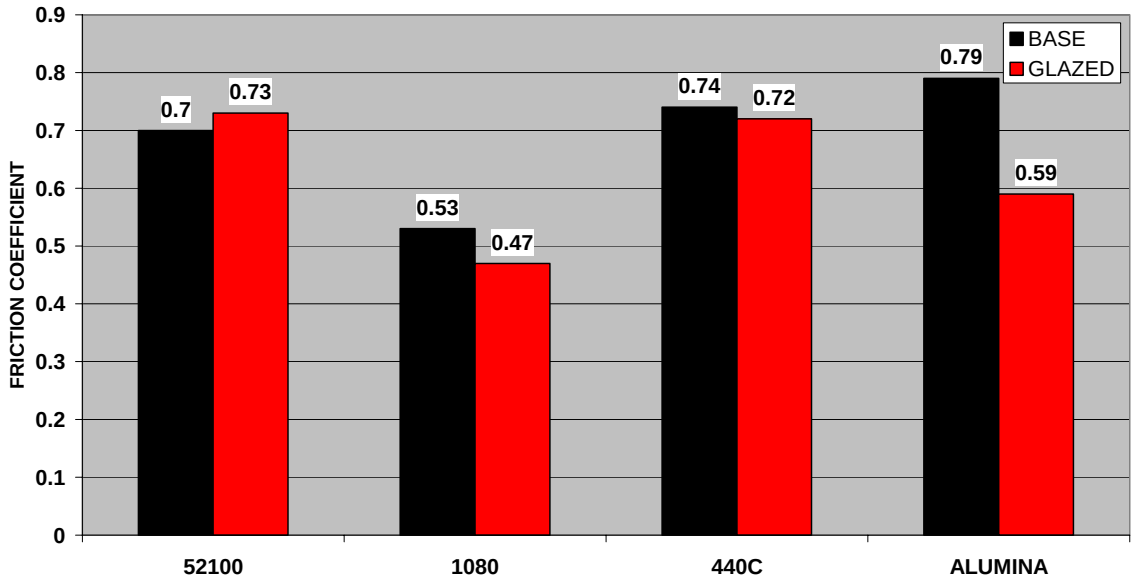

Figure 6. POD friction coefficients of glazed and unglazed steel sliding against various pin materials under dry sliding (Ref 6)

A twin-roller test configuration (Fig. 7) was also used to more closely simulate the rolling contact stresses present at wheel/rail interfaces. The system shown in Fig. 7 was used extensively to simulate the stresses present in 100-ton rail cars. The system is configured to measure the lateral friction forces. Tests were performed with 1045 steel rail and wheel discs that were through-hardened (Rc 40) or glazed. The glazing effectively reduced the friction coefficient from roughly 0.4 for the unglazed condition to 0.3 for the glazed rail rotating on an unglazed 1045 steel counterpart (Fig. 8).

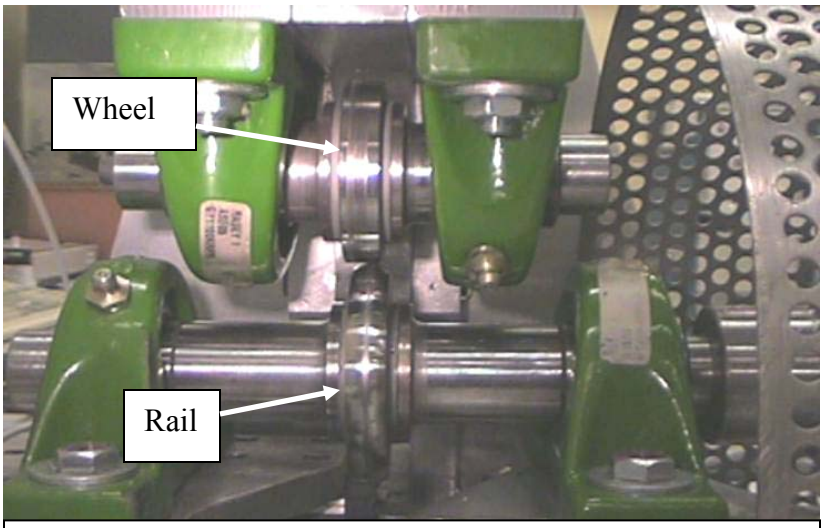

Figure 7. Photograph of LA-4000 twin-roller test rig used to simulate high-contact stresses

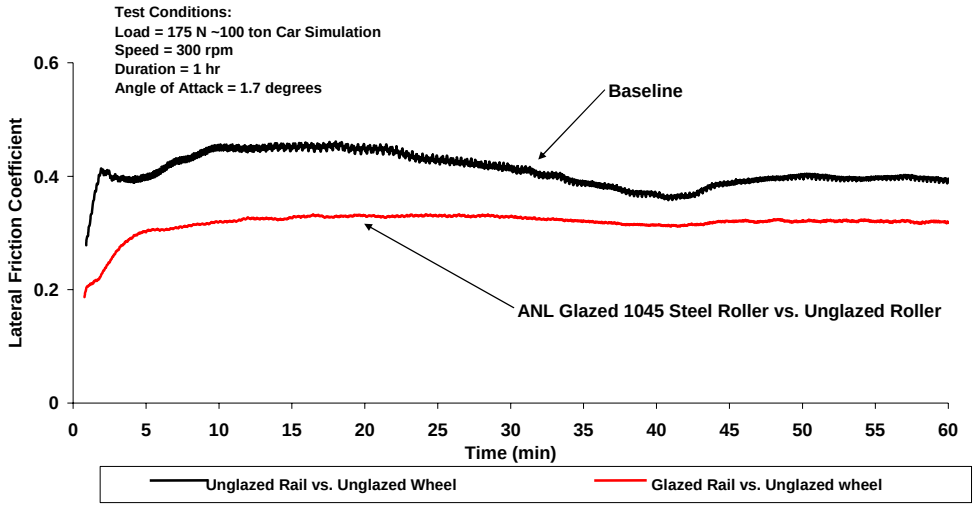

Figure 8. Twin-roller friction data on glazed and unglazed 1045 steel

Similar tests were performed on 1045 steel rollers that were treated with a diode laser by a commercial vendor (NuVonyx). The NuVonyx-treated samples also exhibited lower friction than the untreated steel; however, the low-friction behavior did not endure for as

long as that of the ANL-treated coupons. The difference in endurance is due in part to the fact that the NuVonyx laser treatment was not as well optimized as the ANL treatment.

Tests were also performed to evaluate the durability of the glazed region, in particular to determine if the glazed region would delaminate from the underlying steel. This is a major concern for railroad applications because delamination could be a precursor to the formation of cracks that lead to rail degradation. Long-term (24-48-h) twin-roller tests at a high angle of attack were performed on the twin-roller rig shown in Fig. 7. A 24-h test simulates the passage of ≈1100 100-car trains (each loaded at 100 tons). In all cases, the glazed region remained intact and showed no evidence of delamination.

Microstructural characterization. The microstructure of glazed steel coupons was characterized to determine if a 'white layer' was produced that could account for the reduced friction. Optical and electron microscopy (both scanning and transmission microscopy [SEM and TEM]) were used to characterize the microstructure. Microhardness was also measured, as a function of depth into the substrate in the glazed regions.

Laser treatment of engineering material to modify the surface properties is now a common industrial practice. Surfaces of steel material can easily be heat hardened with a laser beam. Laser glazing, in which the temperature is high enough to melt a region in the surface (as shown schematically in Fig. (9), is a variation of surface thermal

treatment. The melt zone is surrounded by a heat-affected zone in which the temperature is quiet high but not up to the melting point. This surface heating and melting is then followed by a very rapid cooling, leading to rapid solidification of the molten surface layer.

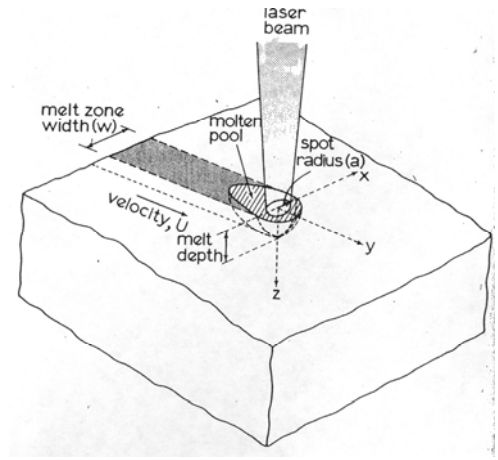

Figure 9. Schematic illustration of laser beam substrate geometry during rapid surface melting and solidification

The microstructural evolution in the laser-glazed layer on 1080 carbon steel surface can be understood from the Fe-C phase diagram shown in Fig. 10, and from the rapid solidification process in plain carbon steel such as 1080. From Fig. 10, we see that the temperature in the melt zone for 1080 steel is greater than 1500°C. Materials in the

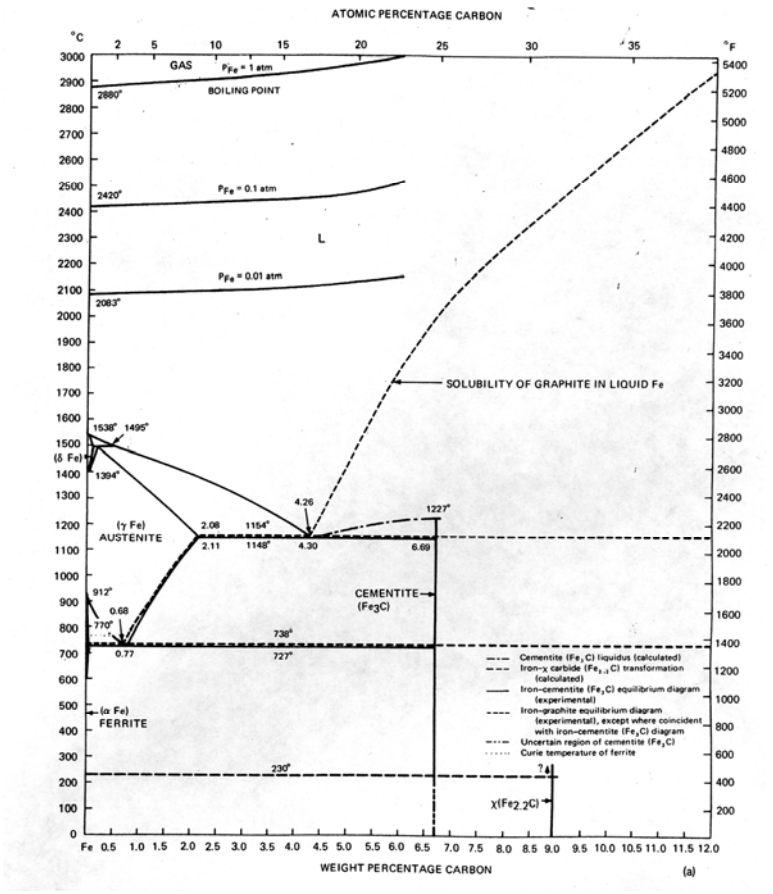

Figure 10: Carbon-iron phase diagram showing eutecoid region; ferrite field, including equilibrium Fe-C, Fe-Fe3C, Fe-Fe2.4C, and delta ferrite field. (J. Chipman, Metals Handbook, 8th ed., vol. 8, Am. Soc. Met., Metal Park, Ohio, 1973, with permission

region below this melt zone (with temperatures between 730 and 1500°C and designated the heat affected zone) are transformed into austenite phase. Materials with a temperature below 730°C retain the original pearlitic microstructure of their base material. With the very rapid cooling (cooling rates of 10^3-10^6 KS^{-1} have been suggested by Ref. 6) of the laser glazing process, the now austenite phase of the heat-affected zone will be transformed to martensite. The liquid pool of the melt zone will also be supercooled and will undergo a nonequilibrium rapid solidification process, producing a

somewhat complex microstructure. Two review papers on weld solidification and rapid solidification (Refs. 6,7) provide some insight into possible microstructural evolution when the melt zone during laser glazing solidifies.

Because of the rapid solidification involved, the composition of the melt as it solidifies remains the same as the base composition, because the time for solute segregation is not sufficient. Also, because the melt pool is in contact with solid material of the same composition, the initial solidification occurs expitaxially in the grains of the base metal. As solidification progresses, some grains with preferred easy growth direction may grow at a faster rate, producing a columnar grain structure. Finally, in the center region, last-to-solidify homogeneous nucleation of new grains is sufficiently easy to allow formation of an equiaxed grain structure. High nucleation density expected in the supercooled region in the center is also expected to produce fine grains. Thus, the microstructure of the center region consists of very fine equiaxed grains.

As the melt zone solidifies, a solid austenite phase is formed, regardless of the grain morphology. Because the cooling rate in the newly solidified region is still high, the "new" austenite is also expected to transform into martensite. Thus, the expected microstructure of the glazed layer on 1080 steel is martensite, but derived from three or four different types of austenite grains. In the heat-affected, unmelted zone, the martensite is derived from the austenite form in the solid state in the base material. In the austenite formed from the melt zone, there is a very thin layer of expitaxial grains,

followed by columnar, grains, and finally, fine equiaxed grains at the centerline surface. A schematic illustration of these various zones and regions is shown in Fig. 11.

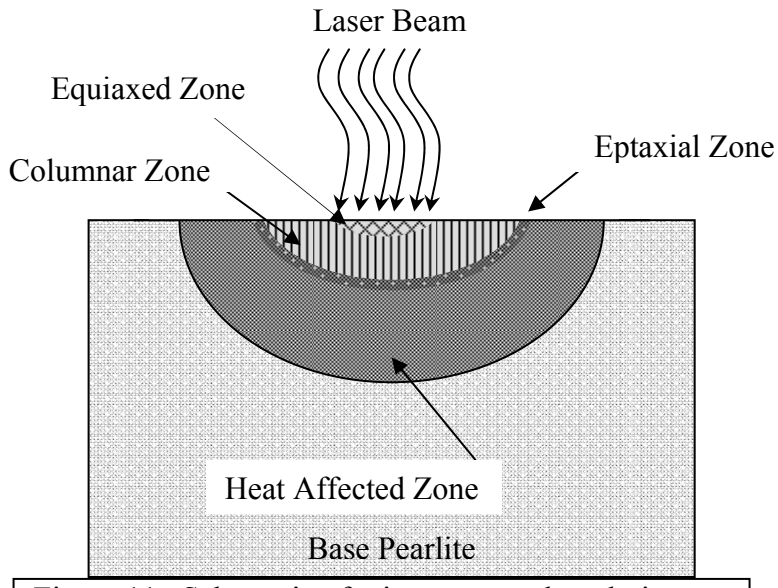

Figure 11. Schematic of microstructural evolution during laser glazing of 1080 carbon steel surface

Samples of glazed 1080 were prepared for the characterization of the microstructure of the glazed layer. Specimens were cut, mounted in bakelite and polished by the conventional metallographic sample preparation technique. The samples were first etched in Vilella's reagent (5% HCl, 95% methanol, 1 g picric acid) to reveal the outline of prior austenite grains in the glazed layer. The samples were later etched in 2% Nital to show the final phases present in the surface layer.

Figure 12 shows the optical photomicrograph of the glazed layer etched in Vilella's reagent to reveal the prior austenite grain boundaries. The austenite grain morphology is consistent with the schematic diagram of Fig. 11. A very narrow region of epitaxial

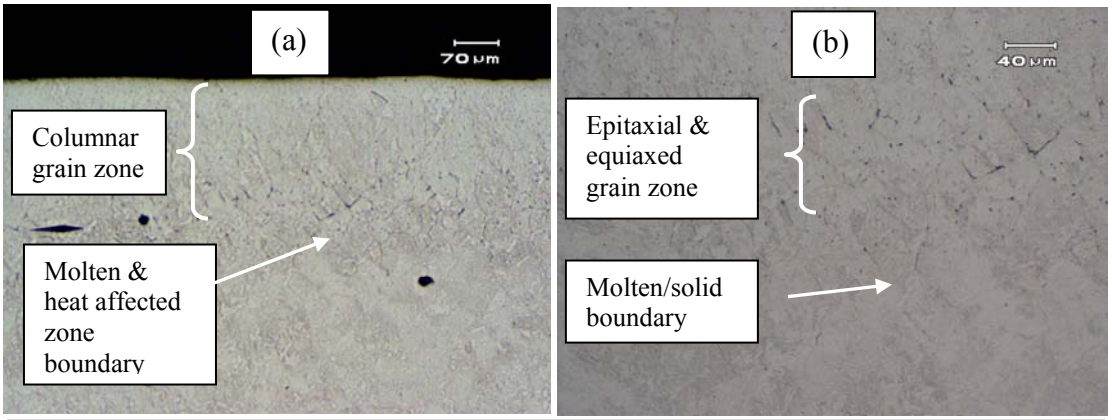

Figure 12 Optical photomicrograph at (a) lower and 9b) higher magnification of laser-glazed layer etched with Vilella's reagent to show outline of previous austenite grain boundaries. (a) columnar morphology of top layer as molten layer solidifies and (b) boundary region between heat-affected zone and molten zone with initial expitaxial grain as solidification begins

equiaxed grains invisible at the boundary of the heat-affected zone and the melt zone, as indicated by the photomicrograph at higher magnification, shown in Fig. 12b. On top of this narrow region is the columnar-grain zone, followed by a very narrow equiaxed-grain layer at the very top surface. Upon the rapid cooling involved in the laser glazing process, all of the austenitic phases that were formed in both the heat-affected zone and the rapidly solidified molten zones (regardless of the austenite grain morphology) are transformed into martensite, as indicated in Fig. 13, optical photomicrograph of the sample etched with 2% Nital. Indeed, after this phase transformation, it is difficult to distinguish between martensite formed from the solidified-molten-layer austenite and the solid-state heat-affected-zone austenite.

Microhardness. The microhardness of samples produced by the ANL and NuVonyx processes was characterized as a function of depth. Figure 4 (from Ref. 8) shows SEM cross sections of ANL-glazed (single-pass and overlapped) rail. The single-pass

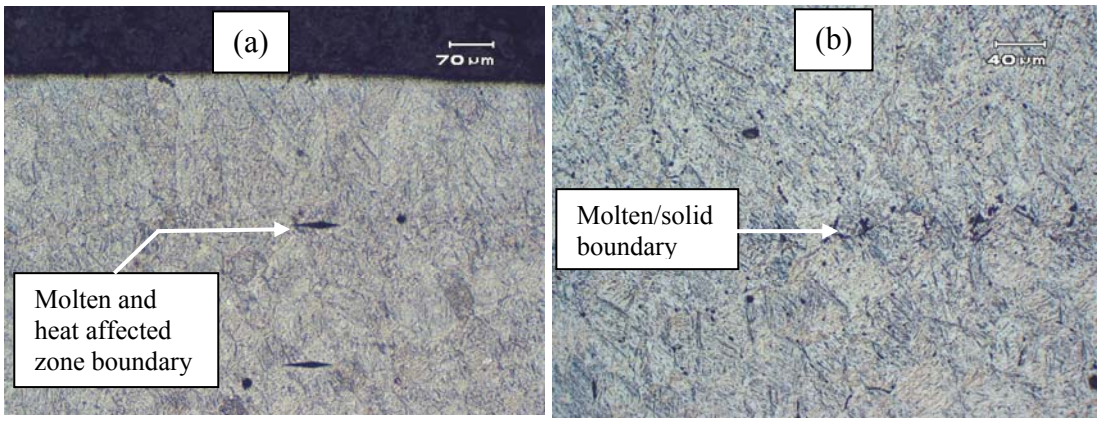

Figure 13. Optical photomicrograph of glazed layer etched with 2% Nital, showing that final phase in both molten and heat-affected zones consists of martensite. (a) top layer of the molten zone and (b) boundary between molten and heat-affected zones.

(nonoverlapped) glazed region registered Knoop hardnesses that ranged from approximately 900 at the surface to a peak value of 1075 further in; in the base steel, the values dropped to 350-400. When the beams are overlapped, some degree of tempering occurs. The results were very consistent from sample to sample, even between samples produced by the ANL process and the NuVonyx process. Figure 15 shows the hardness of a series of 1080 steel bar samples that were treated by the NuVonyx process (4 kW, at two speeds, 2 and 2.5 m/s). The hardness of the 1080 substrate was 350-400 Knoop, increasing to ≈1100 Knoop, decreasing to 800-900 Knoop near the surface.

The glazing process, whether ANL or NuVonyx, produces a hard martensitic phase on top of the base pearlitic 1080 steel. The main difference between the two processes appears to be the thickness of the treated layer. The thickness of the treated region is inversely proportional to the speed. Higher laser-translation speeds produce glazed regions that are thinner, as shown in Fig. 16.

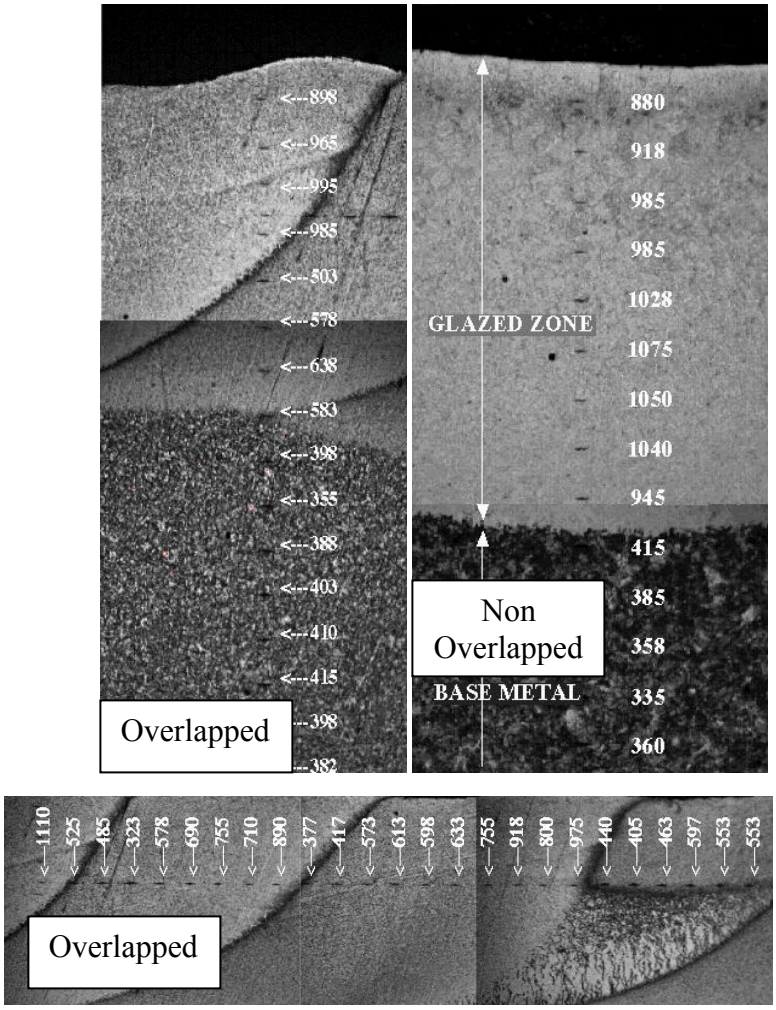

Figure 14 SEM photomicrographs of ANL-glazed rail steel illustrating variation of Knoop hardness with position.

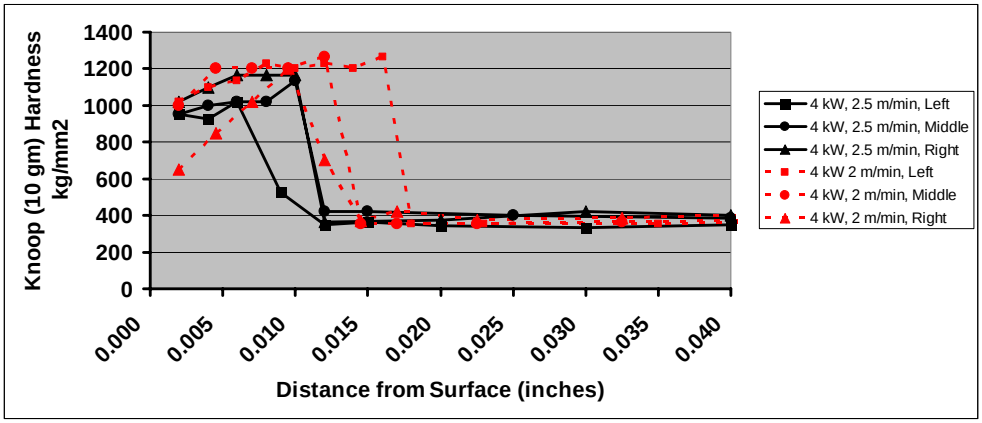

Figure 15. Knoop (10-gm) microhardness of NuVonyx-glazed steel

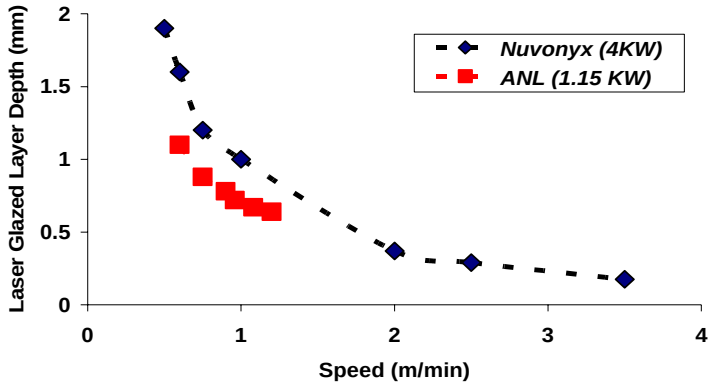

Figure 16: Depth of laser-treated zone as a function of laser speed

Full-Scale Wheel/Roller Tests – Ottawa

The next phase of the research to demonstrate laser glazing as a means to mitigate parasitic energy losses was intended to focus on field studies of laser-treated rails at a facility such as the Facility for Accelerated Service Testing (FAST) (Ref. 9) facility at the Transportation Technology Center, Inc. (TTCI) in Pueblo, Colorado. However, the TTCI raised concerns about installing glazed rail segments in their FAST facility; they were concerned that rolling-contact fatigue might be exacerbated by the martensite structure of the laser-glazed region. Before they would consider placing glazed rail in the FAST loop, the TTCI wanted assurance that the glazed region would not delaminate (or lead to through-rail cracks), which could potentially cause a train derailment.

Ron DiMelfi worked with the TTCI and identified facilities in Ottawa, operated by the National Research Council Canada (NRCC), that are capable of simulating wheel/rail forces with full-scale railroad wheel assemblies. The facility, known as the Wheel,

Bearing, and Brake (WBB) Facility (Ref. 10), is a highly instrumented facility that enables measurements of wheel and rail forces under a wide range of conditions prototypical of freight cars; it uses standard and instrumented wheel sets that run on top of large (63-in. diameter) rims whose profiles replicate the profile of a rail. Discussions with TTCI indicated that the Ottawa facility is capable of providing the types of loading and duration needed to simulate the loads and tonnage that would be experienced on the FAST loop and thus should be able assure TTCI that the glazing process would survive. A contract was subsequently established between ANL and the CNRC (Ottawa) to perform a series of tests to evaluate the friction and durability of laser-glazed rims. A description of the WBB facility, laser glazing of the rim for the Ottawa tests, and results of the Ottawa tests are provided below.

Ottawa Test Facility

A photo of the WBB test facility in Ottawa is shown in Fig. 17. The bottom rims, driven by an electric motor, rotate the top wheel set. The top wheel set can either be a conventional wheel/axle combination that is used on freight cars, or an instrumented wheel set (IWS). The test protocol selected for the Ottawa tests used both types of wheel sets. Initial tests were performed with the IWS to measure wheel/rail friction forces. These tests were followed by long-term tests with a conventional wheel set to put tonnage on the glazed rim/rail, and followed by a final set of tests with the IWS to measure friction forces after the tonnage was applied.

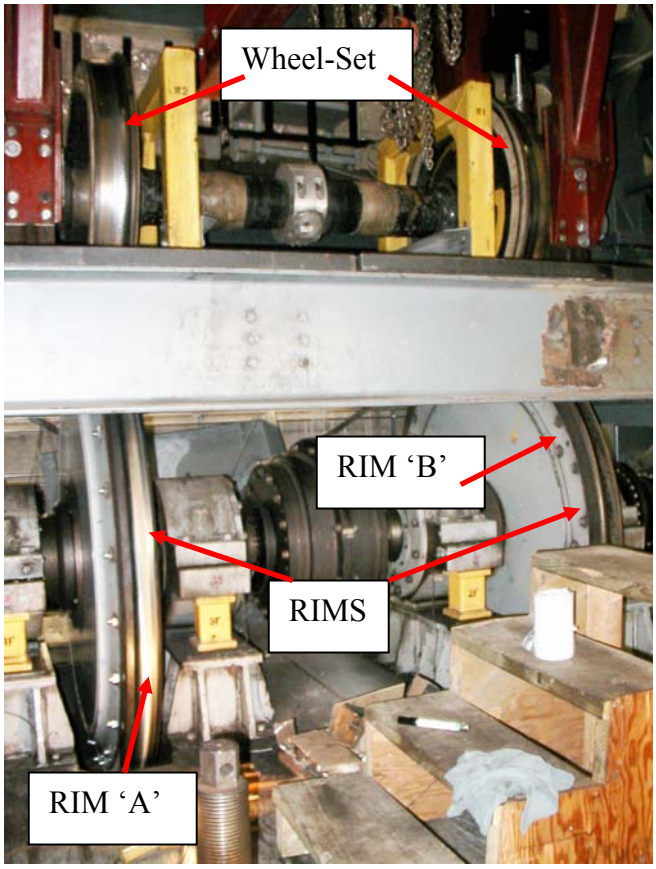

Figure 17. CNRC Wheel, Bearing, and Brake Test Facility

In the tests that were performed, rim 'A' was glazed over one-half of its diameter, while rim 'B' received no treatment.

Laser Glazing of Rim (NuVonyx)

In preparation for the Ottawa tests, two rim segments (each rim is comprised of two 180° segments bolted onto a central hub) were sent to ANL for laser glazing. One segment was used by NuVonyx to optimize their laser processing protocol to produce a glaze comparable to those produced at ANL. This segment was subjected to several glazing treatments and sectioned for metallographic examination (hardness and microstructure).

The second 180° segment was glazed over a 175° arc and was re-assembled with the original mating segment on rim 'A' in Fig. 17. Photos and a schematic representation of the rim profile are provide in Appendix A.

The original plan was to glaze the pink-shaded region of the rim as shown in Fig. 18. For these tests, the glazed region started at the gauge point and was to extend approximately 2-in. onto the top of the rim/rail. In practice, the glazing would not extend this far onto the top of the rail (to avoid potentially low friction on the top of the rail, where traction is critical), but for the purposes of these tests, a wider swath was selected to ensure contact between the wheel and glazed region on the rim.

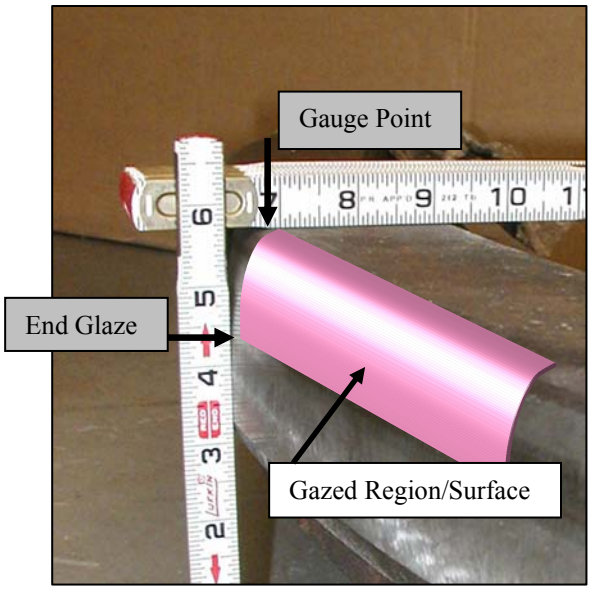

Figure 18. Glazed region on CNRC rim

Because the existing laser facilities at NuVonyx were not adequate to glaze a single 2-in.-wide swath in one pass on the curved rim segment, as illustrated in Fig. 18, we decided to develop a multipass process that would glaze a 2-in.-wide swath by overlapping swaths

that were ½-in. wide. Initial tests with 1080-steel coupons and a short segment of 'virgin' 1080 rail suggested multipass (overlapped) glazing was viable, and NuVonyx proceeded to perform a series of glazing experiments on the sacrificial rim segment to optimize the glazing process. Glazing trials were performed under various conditions (speed, laser power, and beam size) to determine the optimum conditions needed to form a glazed region that was approximately 1-1/2 mm deep; the results presented in Fig. 16 indicate that, at a power level of 4 kW, a translation speed of approximately 0.6 m/min was required. Knoop microhardness data for a series of runs performed at 0.6 m/min on the sacrificial rim are shown in Fig. 19. As seen in Fig. 19, the depth of the hardened zone ranged from approximately 1.5 to 2 mm. The surface hardness was approximately 800 Knoop, compared to previous tests (Fig. 15) that were glazed at faster rates (2-2.5 m/min) on 1080 test coupons, in contrast to the more massive 1080 rim profile.

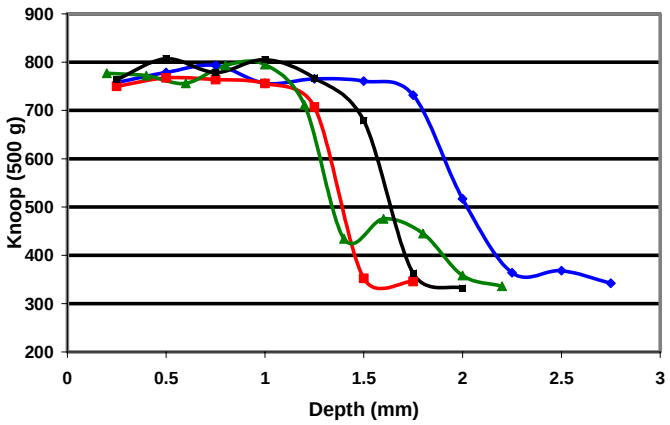

Figure 19. Knoop microhardness of CNRC rim glazed at 0.6 m/min obtained at different locations.

During cross-sectional metallographic examination of segments obtained from the sacrificial rim, several cracks were observed, as seen in Fig. 20. A detailed analysis of

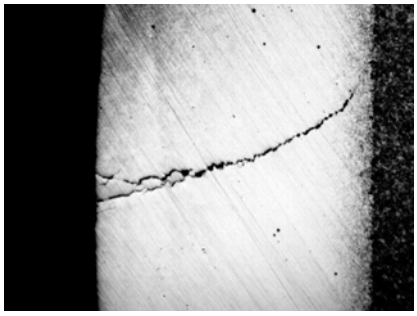

Figure 20. Optical photo-micrograph of 1080 Rim material after multipass glazing treatment at 0.6 m/min. (NuVonyx - ID # - Sample 1)

the cracks (performed by NuVonyx) indicated the cracks only occurred in overlapped (or closely-spaced glazed tracks). Figure 21 shows a Magnaflux photo of three closely spaced, but nonoverlapping laser glazed tracks. Track 1 (Fig. 21) was glazed first, followed by Track 2, and finally by Track 3. As seen in Fig. 21, the cracks were observed between Tracks 1 and 2, and between Tracks 2 and 3. Analysis (Ref. 11) of these cracks and others that were observed in overlapped tracks revealed the cracks only occurred after the second (or subsequent tracks) were glazed (either overlapped, or closely spaced, within 0.5-1 mm).

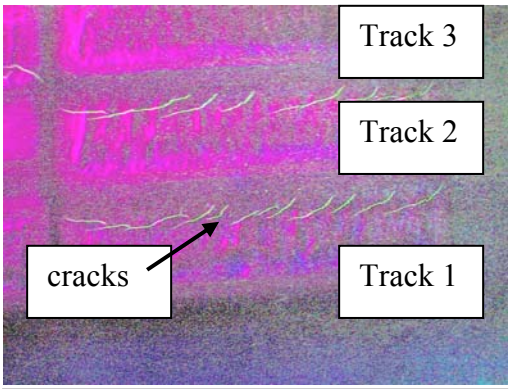

Figure 21. Magnaflux image of closely-spaced, nonoverlapped laser glazed tracks on CNRC WBB trial rim

Analysis of these cracks also revealed the following trends:

- When a region is glazed, the track consists of a well-defined region in which melting of the surface occurred, surrounded by a heat-affected zone (see Fig. 22).
- Cracks form when the subsequent track is placed too close to the previous glazed track.
- The occurrence of the cracks may be significantly influenced by residual stresses in the base material (the rims used in these tests were not freshly ground; they had been used by the CNRC in previous tests and therefore contained residual stresses in the near-surface regions).
- Cracks were not observed in single, widely spaced (>1 mm) tracks, in which the heat-affected zones did not overlap.
- The occurrence of cracks in 'virgin' rail segments (Fig. 22) or 1080 steel coupons was extremely rare, even in cases where the glazed regions overlapped (albeit at faster glazing speeds of 2-2.5 m/min).

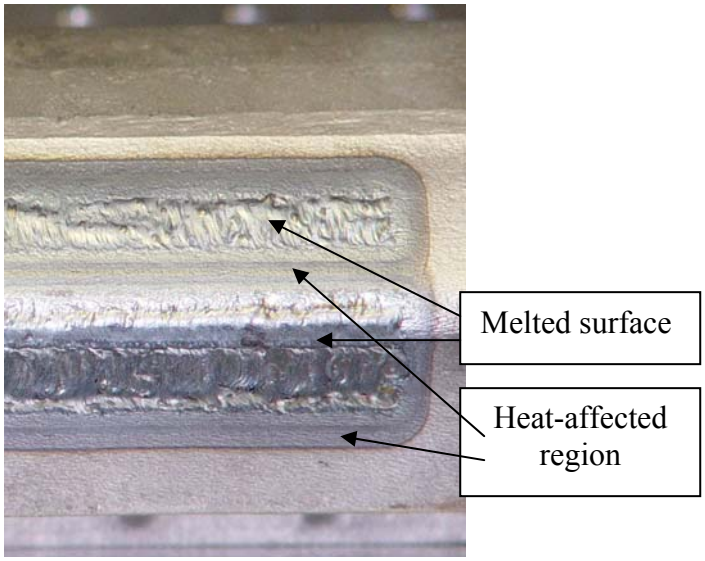

Figure 22. Photograph of glazed 'virgin' 1080 rail glazed; heat-affected zones overlapped

The trend that NuVonyx observed in the glazed regions when tracks were either overlapped or closely spaced is shown in Fig. 23. After the first pass, no cracks occur. The subsequent track (Pass 2) produces a back-tempered zone, and cracks are observed just outside of the back-tempered region in the prior (Pass 1) track.

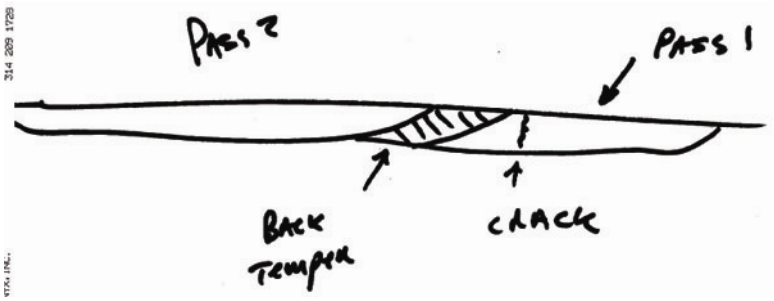

Figure 23. Schematic representation of crack location in closely spaced (or overlapped) laser-glazed tracks

To avoid the cracks that were plaguing attempts to produce a wide (2-in.) swath of laser glazed rim (as shown in Fig. 18, we decided to glaze two, approximately ½-in.-wide tracks, on the rim, with one track centered on the gauge point (see Fig. A.2), and the second track spaced approximately 10-12 mm from the first track on the top of the rim. Pursuant to a teleconference on Feb 11, 2004, NuVonyx glazed another test segment to determine if moving the top-running-surface glazed region closer to the gauge glazed region would produce cracking in the region between the two glazed regions. Previously, the heat-affected zones of the gauge and top-running-surface glazed regions were separated by 10 mm. Ottawa indicated that better alignment of the top-running surface glazed region would be obtained if the top glazed region was 3 mm closer. We asked NuVonyx to perform another trial run (and Magnaflux) to determine if cracks formed when the glazed regions were closer (approximately 7-mm separation). They performed

another run with a separation between the heat-affected zones of approximately 6 mm. No cracks were observed.

NuVonyx was given the go-ahead to treat the final rail segment if the trial runs were crack free); they subsequently glazed the final rail segment with the closer separation and magnafluxed the entire rail segment. Overall, the glazing was a success. Relatively large cracks were observed at the ends of the rail segments where they mate up with the other 180-degree segment. However these cracks are in regions that were not glazed and are believed to have been present before the glazing operation. Two very small cracks (approximately 2 mm long) were observed in one isolated region in the top running surface glazed region.

Figure 24 shows a photograph of the second rim after it was glazed; the inset shows the appearance of the two small 2-mm-long cracks that were observed in the glazed region on top of the track. Figure 25 shows a close-up of the glazed rim (mounted on the Ottawa WBB test rig). The location of the glazed tracks is also noted in Fig. 25.

After the glazing treatment by NuVonyx, the glazed rim was returned to Ottawa where it was reassembled with its mating rim segment and mounted on the WBB test rig for tests that were performed the week of March 22, 2004.

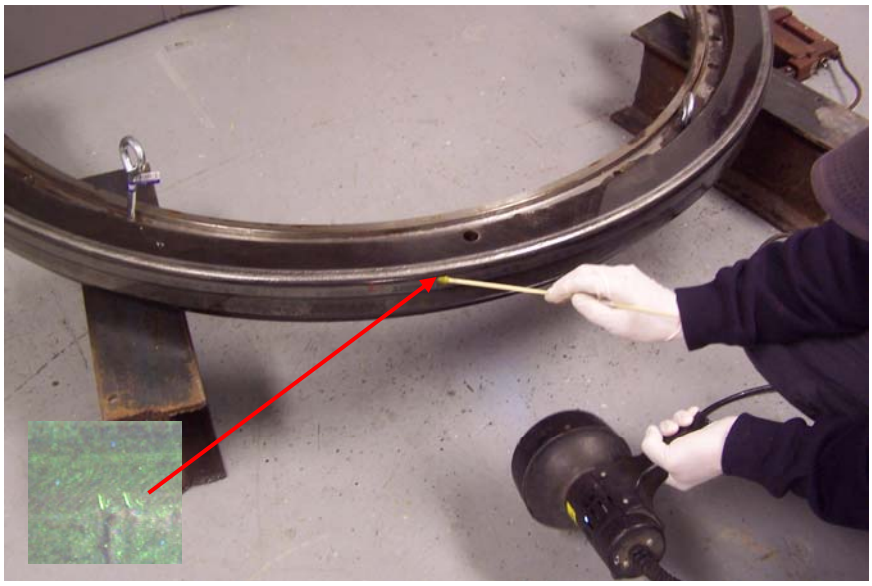

Figure 24. Photograph of glazed rim, and magnaflux image of two small cracks

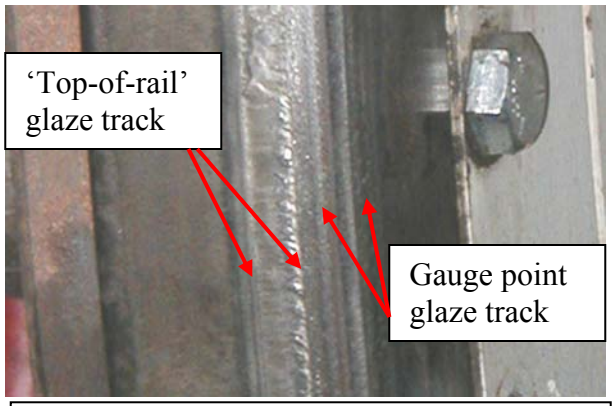

Figure 25. Close-up photograph of glazed rim

Ottawa Tests on Glazed Rim

The Ottawa tests were performed under contract to the Canadian National Research Council Centre for Surface Transportation Technology in Ottawa, Ontario (ANL contract # 3F-01841). The following CNRC staff participated in the tests: Michael Krzyzanowski (Rail Business Manager), Philip Marsh (Project Engineer), Ron Koopman (WBB Facility

Manager), and Thomas Davies (WBB Facility Operator). Appendix B provides an overview of the WBB facility and describes the forces that are measured during the test. Preliminary results from the tests can be found in Ref. 12.

The glazed rim was returned to Ottawa for tests designed to confirm that the glazing reduces the friction and to demonstrate that the glazed region would be sufficiently robust to warrant field tests without undue concern about causing a derailment. The glazed segment was reassembled with its sibling rim segment and installed on the WBB test rig. The sequence of runs is shown in Table 1.

Table 1. Sequence of Ottawa tests on glazed rim

Run Sequence	**Mon.**	**Tue.**	**Wed.**	**Thurs.**	**Fri.**
1a – 1d: IWS friction measurements @ 10,000 lb, 6 mph. Replicas 1-0, 2-0, and 3-0	■				
Change-over to standard wheel set Replicas 1-1, 2-1, and 3-1		■			
2a-2b: Initiate heavy-load runs @ 33,000 lb, 30 mph		■			
3a-3d: Continuation of heavy-load runs @ 33,000 lb, 30 mph			■		
4a-4b: Heavy-load runs; last run (4b) at high yaw/flanging Replicas 1-3, 2-3, and 3-3 and mag flux				■	

Change-over to IWS				[redacted]	
5a-5c: IWS friction measurements @ 10,000-33,000 lb and 6-10 mph					[redacted]

Further details of the individual runs are summarized in Table 2

Table 2. Load, speed, and MGT data

Run No.	Vertical Load (lb)	Speed (mph)	Duration (s)	Approximate MGT[a]	Comments
1a	10	6	1100	0.0029	Tangent @ 6 mph and yaw axle – some oil on rollers
1b	10	6	675	0.0018	Start on tangent @ 6 mph and yaw axle
1c	10	5.8	630	0.0016	Increase yaw to run on glazed area in the flange
1d	10	6	910	0.0024	Use lateral actuator to keep axle on glazed surface, then yaw
2a	10	31	785	0.0107	Adjust for regular wheel set
2b	35	31	710	0.034	Yaw to run on top glazed surface
3a	35	31	2340	0.1121	Run on top glazed surface
3b	35	31	3937	0.1887	Readjust and run on glazed surface
3c	35	31	2366	0.1134	Readjust and run on glazed surface
3d	35	31	3840	0.154	Readjust and run on glazed surface

4a	35	31	6800	0.3259	Run on glazed surface
4b	35	31	150	0.0072	Run on glazed surface
4c	35	31	367	0.0176	Yaw to run on flange
4d	36	31	1130	0.0557	Yaw to run on flange
5a	10	6	350	0.0009	Start on tangent @ 6 mph and yaw axle
5b	18	10	350	0.0028	Increase speed and vertical load and yaw axle
5c	38	11	275	0.0051	Increase speed and vertical load and yaw axle
5d	38	11	100	0.0018	Yaw axle to run on flange
[a]Total approximate MGT on roller				**1.07**	

The first four tests (1a-d) was performed with the IWS to provide friction data on the glazed (and nonglazed rim segments) at the beginning of the test, before any tonnage was applied to the glazed rim. Data were collected at 200 Hz, sufficiently fast to discriminate between the glazed and unglazed rim segments on Rim A (Fig. 17). Runs 1a-d were performed at a loading of approximately 10,000 lb at a speed of 6 mph. Early Tuesday morning, the instrumented wheel set was removed and a standard wheel set was installed for the next three sets of runs, (runs 2, 3, and 4, Table 1). During runs 2, 3, and 4, the speed was increased to 30 mph, and loads (on each wheel) were increased to 33,000 lb. Runs 4a and b were subjected to a high yaw to induce contact along the glazed track, positioned at the gauge point on the rim. Late Thursday, the standard wheel set was removed, and the instrumented wheel set installed for a final set of runs (5a-c) to measure

the friction after the durability runs (runs 2 – 4). Runs 5a-c were performed at speeds that ranged from 6 to 10 mph, at loads that ranged from 10,000 to 38,000 lb.

Friction. One of the major goals of the Ottawa tests was to confirm earlier AAR and laboratory tests that indicted a lower friction coefficient for glazed steel. The IWS used in Runs 1a-d and 5a-d provided data on orthogonal forces experienced by each wheel of

$$\text{Friction Coeff} = \frac{\{(\text{Lat.})^2 + (\text{Long.})^2\}^{1/2}}{\text{Vertical Force}}$$

the IWS, where the lateral (Lat.), longitudinal (Long.) and vertical (Vertical Force) forces are defined in Appendix B. Data recorded at 200 Hz (0.005-s intervals) during these runs were used to calculate the friction coefficient from the following relationship (see appendix C for more details).

An example of the force behavior is shown in Figs. 26a-c (for Run 1b). Run 1b was performed with a load of 10,000 lb at a speed of 6 mph. Initially, no yaw was applied (comparable to running on tangential track). Then, the yaw on the top IWS was gradually increased (between t = 100 and 450 s), leading to an increase in the magnitude of the lateral and longitudinal forces.

Figures 27 and 28 show the friction coefficients that were measured during Run 1b. Figure 27 shows the friction during the entire run, whereas Fig. 28 shows the friction during the time interval between 250 and 260 s. The top trace in Fig. 28 is the applied

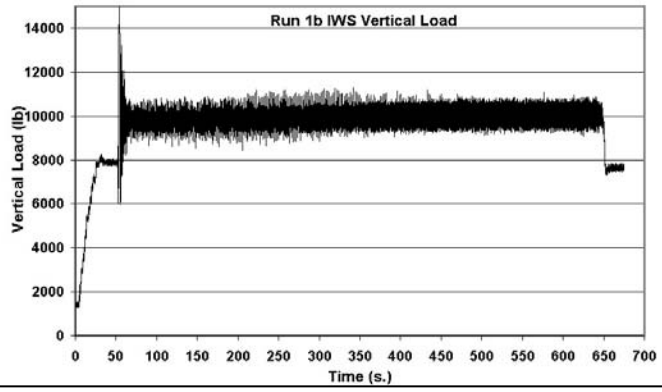

Figure 26a. IWS vertical force history during Run 1b

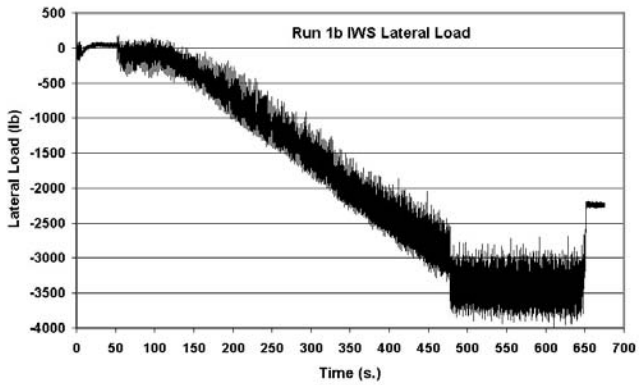

Figure 26b. IWS lateral force history during Run 1b

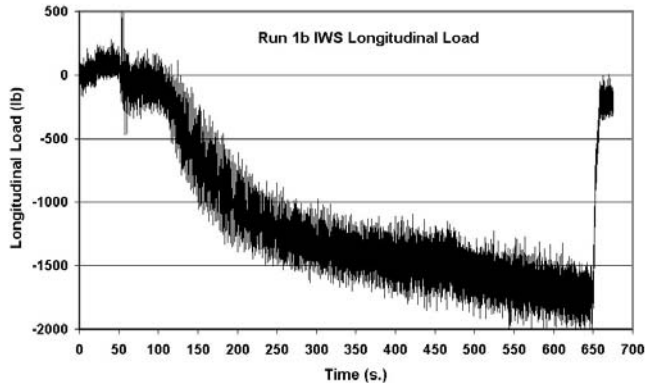

Figure 26c. IWS longitudinal force history during run 1b

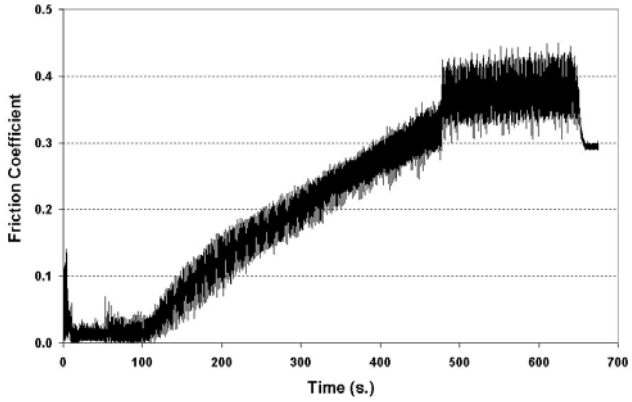

Figure 27. Friction during Run 1b

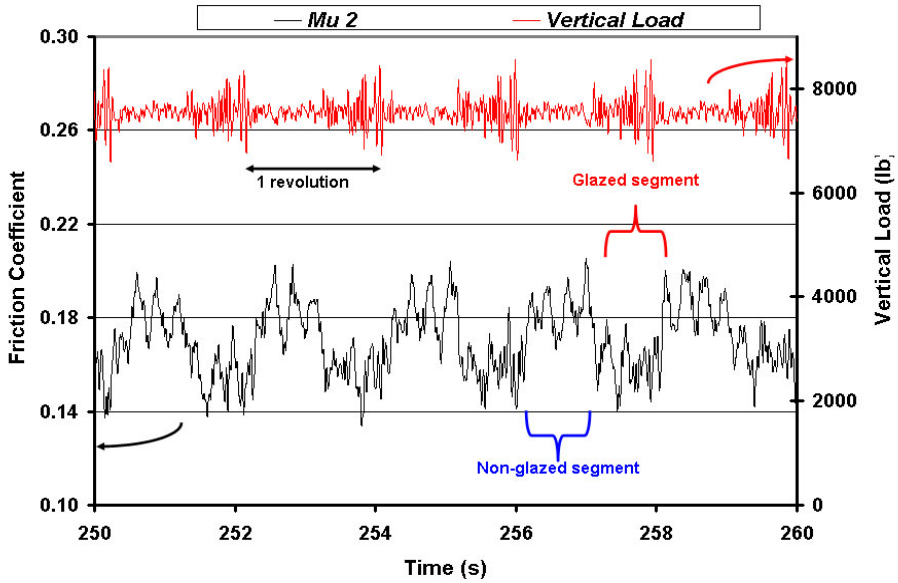

Figure 28. Friction and WBB vertical load between 250 and 260. The '1-revolution' arrow in Fig. 28 represents the time for the bottom rim (one-half of which was glazed) to complete one revolution (approximately 1.9 s for the 63-in.-diameter rim running at 6 mph). seconds during run 1b.

vertical load, as measured with the WBB force transducer (the true vertical load as measured on the IWS wheel set is closer to 10,000 lb, which includes the weight of the IWS wheel set). The vertical load trace in Fig. 28 shows a relatively smooth segment followed by a rougher trace. The rougher trace segments corresponded to time when the glazed rim segment was in contact with the IWS wheel – which was readily audibly correlated with the slow (6 mph) runs. The noise level produced by the WBB rig significantly increased when the glazed rim rolled under the IWS. The increased noise (and rougher vertical load trace) was somewhat fortuitous; it made it relatively easy to determine whether IWS was on the glazed rim segment or on the nonglazed rim segment.

The friction trace in Fig. 28 shows a cyclic behavior, depending on whether the IWS was in contact with the glazed or nonglazed rim segments. For the time segment shown in

Fig. 28, the glazed rim exhibited a 13 % reduction in friction. More detailed analysis of the friction reduction observed in run 1b is shown in Fig. 29 which summarizes the reduction (normalized to the nonglazed rim) for various time periods during Run 1b. The reductions were determined from averages of the friction from the glazed and unglazed rim segments. As seen in Fig. 29, the reductions ranged from approximately 40% (for the 130-140 s interval) to approximately 8% at high yaw values. Appendix D (Figs.D23-D27) contains similar data for Runs 1c, 1d, 5a, 5b, and 5c.

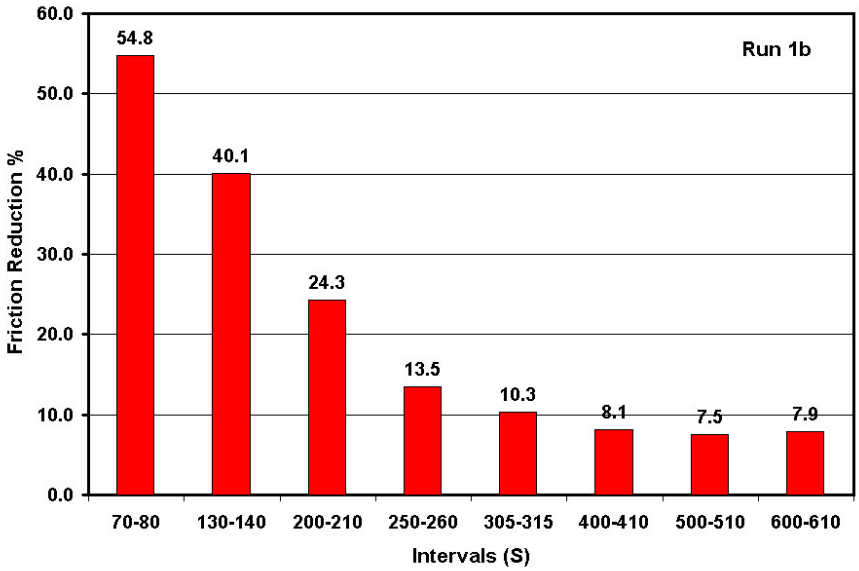

Figure 29. Friction reduction on glazed rim (normalized to the unglazed rim segment)

Friction was measured at the end of the long-duration tests to determine if the friction reduction remained, i.e., would the glazed region wear and if so, would the same level of friction reduction remain? After the last long-duration run (4d), the IWS was reinstalled and another series of tests was performed. Run 5a was performed under the same conditions as Runs 1b-d (10,000 lb and 6 mph). The data in Appendix D (Figs. D15 and

D16) indicated a cyclic friction response comparable to that for Run 1b, but not as pronounced. Additional tests were performed at higher loads and slightly higher speeds. Figures 30 and 31 show the friction data for Run 5c (38,000 lb and 10.7 mph). A cyclic friction response is again observed (with a period consistent with the 10.7 mph rotation speed, 1.05 s/rev). In this case the cyclic behavior is more pronounced than the behavior at lighter loads (Run 5a).

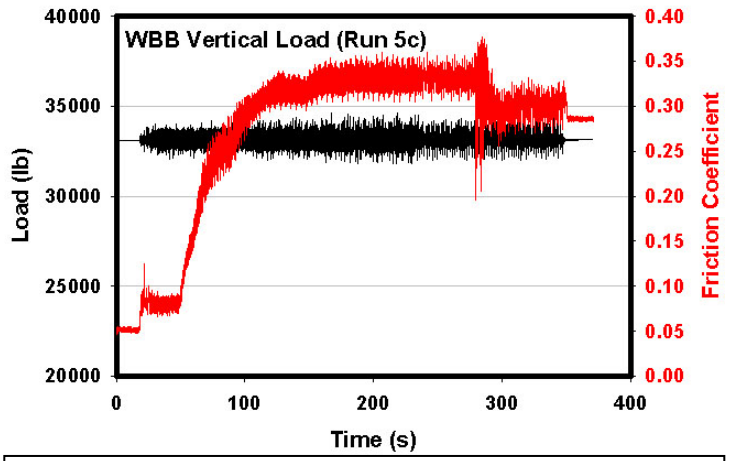

Figure 30 Friction and IWS lateral load during Run 5c

Optical microscopy of glazed regions. Digital images and replicas were taken at various times during the runs to document changes in the morphology of the glazed regions. Analyses of these images and replicas provide important information on how the glazed region performed, including

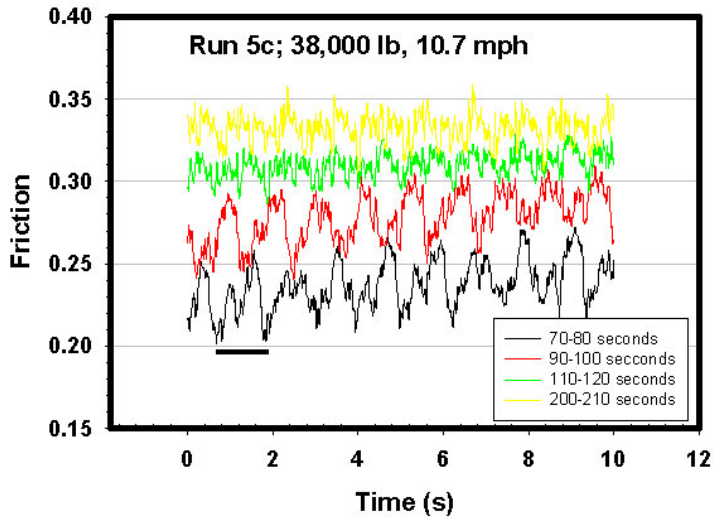

Figure 31. Friction during various 10-s intervals of Run 5c

- the degree to which the two laser-glazed tracks participated in the tests, i.e., were both tracks active in reducing the friction
- the degree to which a given track contributed to the lateral forces, i.e., how wide was the glazed region where compared with the width of the true contact area
- the effect the surface finish/roughness of the glaze had on the actual area of contact, i.e., what is the real area of contact, and how does this relate to the friction reduction mechanism?
- the occurrence of fatigue cracks during the long-term tests, i.e., did cracking occur, and if so did it propagate?

Figure 32 shows a montage of photos of the glazed rim installed on the WBB test rig. The areas within the red boxes highlight the appearance of the two tracks to which NuVonyx applied a glaze. At various intervals during the runs, a patch of white spray

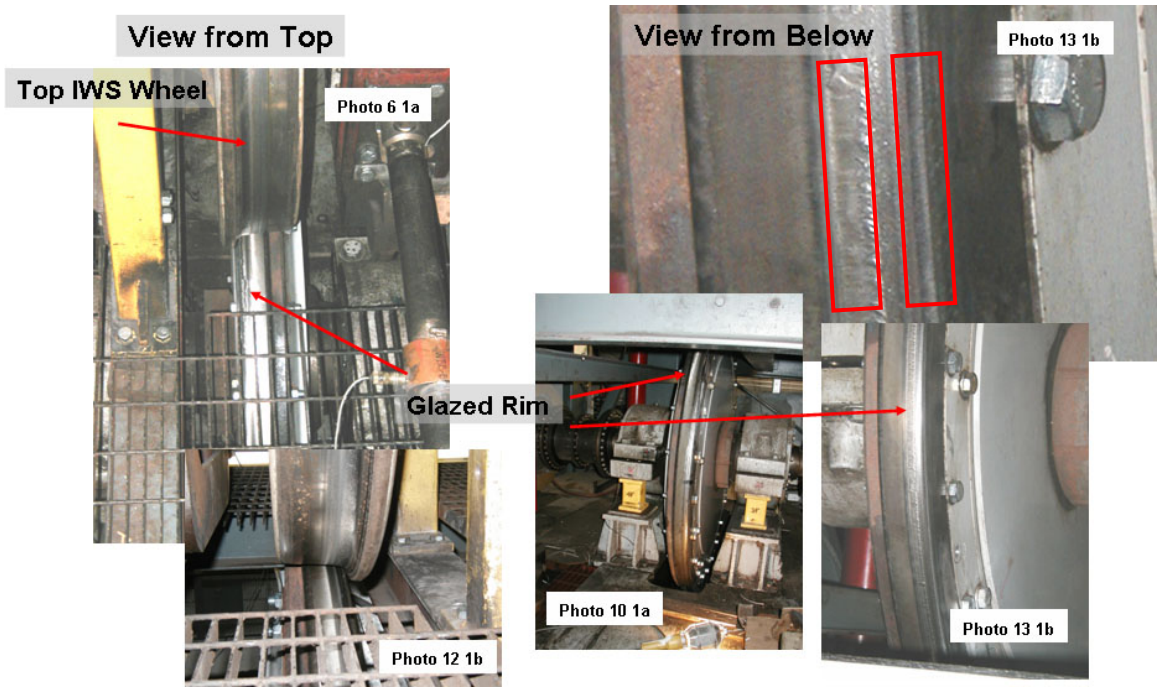

Figure 32. Montage of photos showing appearance of glazed rim. Areas within red box ('View from Below') show the two glazed tracks

paint was applied on various segments of the glazed tracks. The rig was started up again and allowed to run for a minute or two; it was then inspected to see where the paint was removed contact between the two wheels. Figure 33 shows photographs that illustrate the concept and how the contact area appeared after Run 4a. A close-up of the glazed region near the beginning of the long-term runs is shown in Fig. 34.

As seen in Fig. 34, the amount of white paint in the glazed track is a substantial fraction of the area. In contrast, a large fraction of the white paint has been worn off of the glazed track in Fig. 33. At the beginning of the long-term (high-load) runs, the wheel set was apparently running on the tops of asperities in the glazed tracks. As time progressed during the runs, the top wheel set (which is considerably softer than the glazed material)

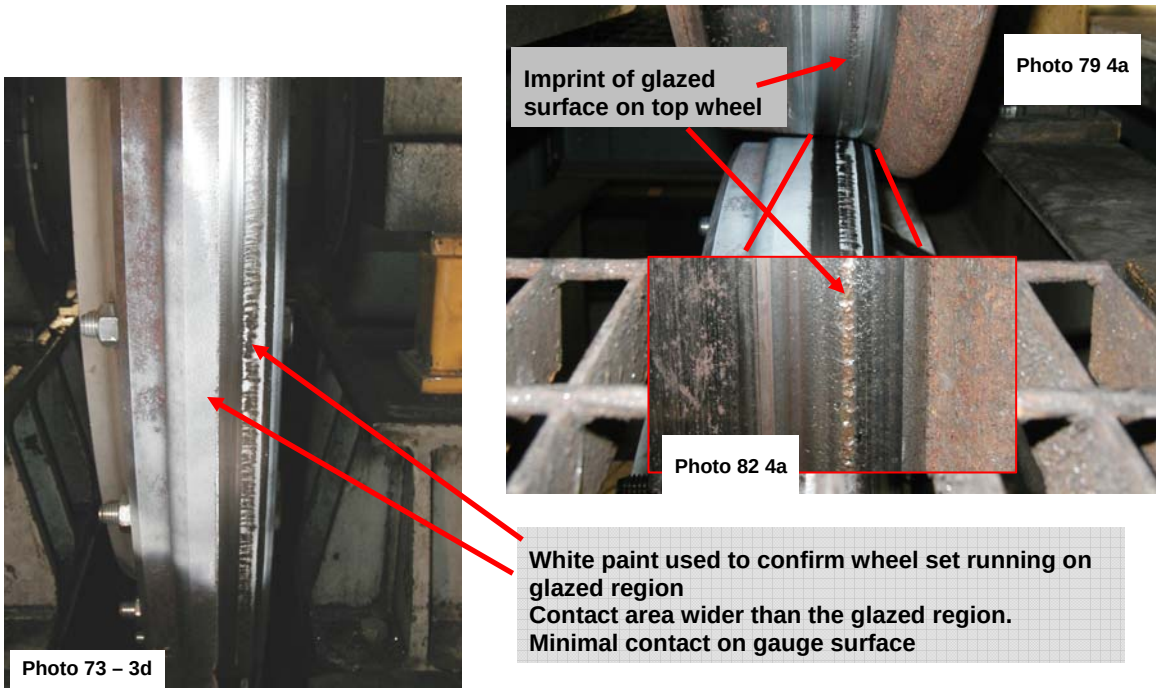

Figure 33. Appearance of glazed rim and wheel contact area after Run 4a

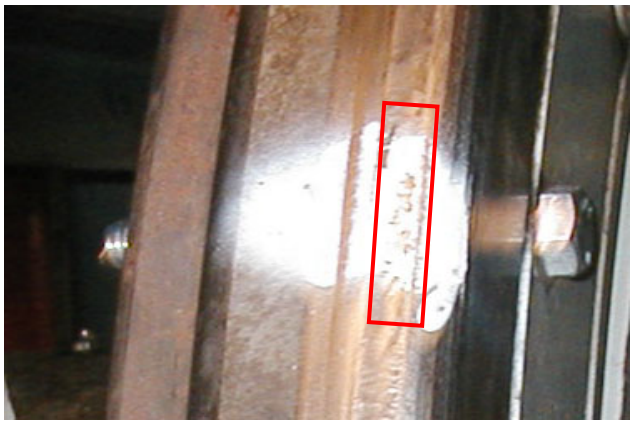

Figure 34. Photograph of glazed track at start of long-term tests

gradually wore away to conform to the shape of the glazed region. The inset photo in Fig. 33 (photo 82 4a) illustrates the degree to which the wheel set has been worn to accommodate the harder glazed material.

Figure 35 shows photograph of the glazed rim after run 4d. The red arrow in Fig. 35 shows the width over which contact was made during the long-duration runs. This width is approximately three times the width of the top glazed track. The glazing treatment applied to the gauge region apparently did not contact the wheel set during the runs.

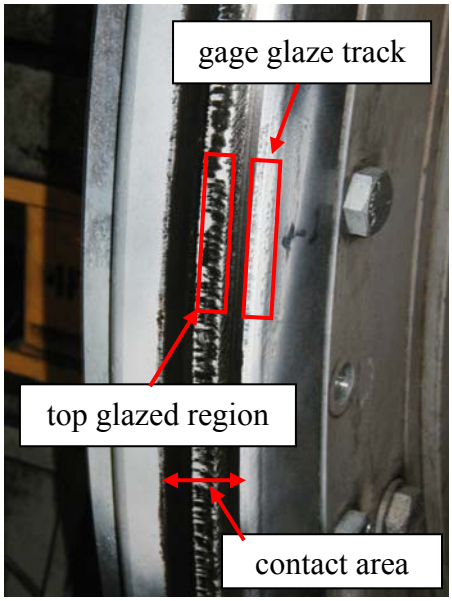

Figure 35. Photograph of glazed rim after Run 4d

While the IWS wheel set was being reinstalled for Runs 5a-d, a magnaflux treatment was applied to the glazed rim segment to determine if fatigue cracks occurred. Appendix E shows photographs taken after the magnaflux treatment. The photographs show the presence of microcracks, but not necessarily in the glazed tracks. Most of the

microcracks occurred just adjacent to the top glazed track, on the side facing the gauge point. No cracks were observed on the other side of the glazed track. One instance of pull-out was observed in the glazed track (see Fig. E2); however, replicas of the glazed rim taken at various times during the Ottawa tests suggest that the region that experienced the pull-out may have experienced abnormally high stresses due to the roughness of the glazed track. The pull-out region was, in essence, a point sitting high above adjacent regions, and thus was supported by a major fraction of the applied load.

In addition to the magnaflux photographs in Appendix E, replicas were obtained at three locations at various times during the Ottawa tests. The results are presented in Appendix F. The images in Appendix F confirm the presence of microcracks at the three locations just before Run 5a, similar to the microcracks observed during the magnaflux treatment (also performed just before Run 5a). The replicas obtained before Run 3a, however, do not show the presence of microcracking; thus, the microcracking occurred at some time between Runs 3a and 4d, a rather wide time window. Replicas were not taken at intervals between Runs 3a and 4d, and thus the onset of the microcracking cannot be more precisely pin-pointed.

Summary and Discussion

The friction data presented in appendix D demonstrate that laser glazing produced a surface layer that led to lower friction forces between the wheel and rail material, and that the glazed region, overall, remained intact. Figures D22-D27 show the reductions in friction coefficient at various time periods during Runs 1 and 5. The largest reductions

were observed during Runs 1 b-d, where reductions ranged from 5 to 40%. At the end (Runs 5a-c), the friction reductions ranged from 4 to 40%. Analyses of the glazed tracks indicate that contact occurred primarily between the wheel and the glazed track on the top of the rail, not between the wheel-flange and the glazed region along the gauge point on the rail. The one exception to this general condition would be in situations where a large yaw was applied to the wheel sets. When contact was made under large yaw, the friction increased dramatically, and the difference between the glazed and nonglazed rim was reduced.

There are several possible mechanisms that might explain the observed friction reductions in glazed surfaces. One view might be that the friction between the wheel and untreated rail is a reflection of the work expended in the plastic flow of the rail, the storage of elastic strain energy in the form of dislocations, and the work of fracture along that subsurface deformation layer. Such a model would be framed in the context of a delamination-wear mechanism. In the case of laser glazing, the thin glazed surface is melted and very rapidly re-solidified. The result can be a very fine grain structure and a very fine distribution of carbides, i.e., finer than exists in the normal rail microstructure and in conventionally hardened-and-tempered steel. Glazing the surface results in a graded microstructure that can reduce friction and wear by resisting plasticity at the surface. The softer sub-layers provide a tougher, more forgiving, material that resists brittle fracture. The sub-layers are exposed to lower stress levels, and are thereby less likely to plastically deform. Therefore, the entire glazed microstructure may offer a durable, friction-reducing surface.

Another explanation of why our glazed surfaces experience reduced friction is based on an adhesive wear mechanism, and comes from the macroscopically rough surface that is produced on our laser glazed rail steels. Figure 36 qualitatively illustrates this mechanism. The mechanism is based on the premise that the real area of contact between the wheels and rims for the glazed rim segments was significantly smaller than the real area of contact for the non-glazed rim segment. Under sliding/rubbing conditions, the friction force that resists relative motion between two bodies is typically assumed to be proportional to the real area of contact (A_c) and a constant force per unit area (s) resisting the motion (Ref. 13):

$$F_f = A_c * s$$

For adhesive friction, s is often taken as the critical shear stress. Differences in either s, or

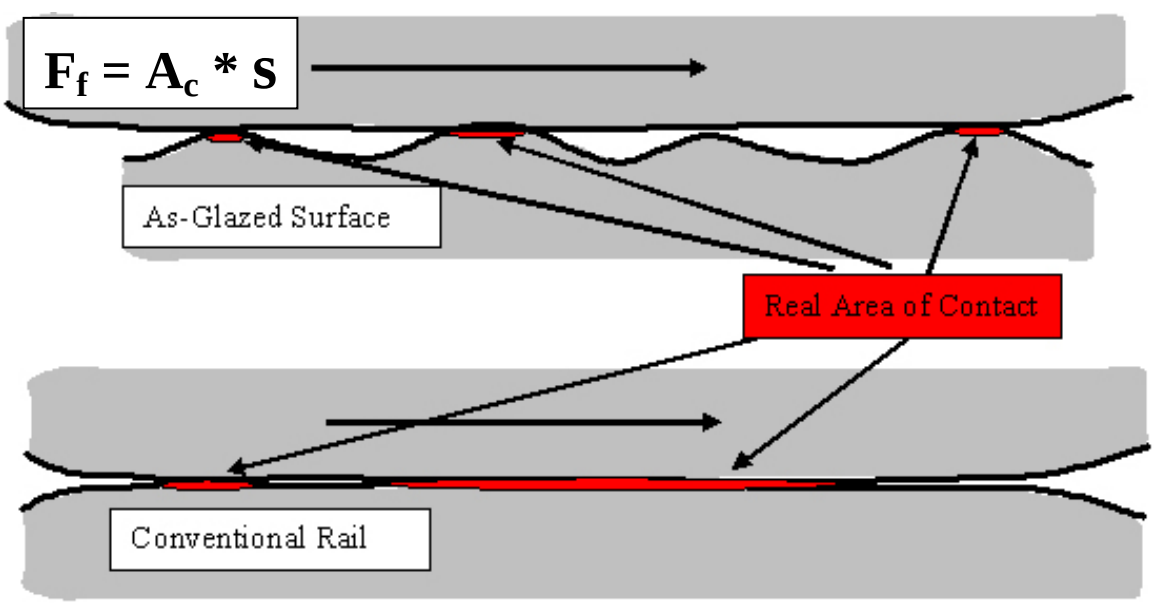

Figure 36. Effect of surface roughness on real area of contact

A_c could account for the reduced friction force (and hence the friction coefficient). Microhardness measurements by Lojkowski et al. (Ref. 14) indicate that the hardness of near-surface regions of worn rail varied as a function of depth. The 1070 rail steel that Lojkowski et al. examined was approximately 4 GPa (in good agreement with the 400 HKN measurements shown in Figs. 9 and 10 for the bulk regions of the glazed samples). Closer to the surface (in a region approximately 100-µm deep), the microhardness ranged from 10 to 14 GPa (at the surface). Thus, the critical shear stress for either the glazed steel (where Figs. 9 and 10 show hardnesses of 1000 to 1200 HKN), or a worn (nonglazed) rail steel should be similar. Therefore, assuming that an adhesive wear mechanism is operative, this observation leaves Ac as the major factor that affects the friction response. For the conventional rim segment, the surface was relatively smooth, with a surface finish on the order of 1 µm Ra. In contrast, the glazed regions were significantly rougher; the spacing between the peaks (illustrated in Fig. 36), which were readily visible to the naked eye, were on the order of 2-5 mm. Thus, the peak-to-valley height, the lower real area of contact, as illustrated in Fig. 36, could account for the lower friction in the glazed region, rather than by a material microstructure change produced by glazing.

A related effect was observed in recent studies on laser-clad rail track by Hiensch et al. (Ref. 15), who reported the rolling-contact-fatigue behavior of rail modified by a laser cladding process developed by Duroc (Ref. 16). The laser cladding process was applied to fuse/mix a second compound into gauge regions of a rail. The laser-clad regions were subjected to field tests in an as-deposited state and remained intact. The authors indicate

that the first year of field testing identified the need to reprofile (grind) the laser-clad region in future tests to mitigate the formation of surface cracks that can develop due to high peak stresses. However, they did not address the frictional response of their coating as related to its as-produced rough surface (their laboratory-scale twin-disc tests that addressed friction/traction and rolling contact fatigue were performed on unclad, or clad aand ground test coupons). The Duroc process is a two-material process. On the issue of surface cracks, as-produced laser clad surfaces may behave differently than as-produced laser glazed surfaces, which only involve the rail steel. In general, grinding either treated surface is, of course, efficacious so long as a sufficient amount of the material that improves properties remains.

Recommendations

Results of the Ottawa tests confirmed that laser glazing can indeed reduce friction between wheel and rail surfaces. Such a reduction can have significant implications for reducing parasitic losses and thereby improve the fuel efficiency of rail transport. Although this bodes well for the concept of developing laser glazing as a means to treat critical regions of rails, implementing this strategy will require further investigation that includes

- Field studies on treated rail segments in an instrumented environment sufficiently long to accumulate 50-100 MGT exposure.
- Full-scale and/or field studies that are performed on as-glazed and as-glazed-and-ground/reprofiled rail segments

- Development of laser-processing protocols to enable single-pass treatment that avoids back-tempering of glazed regions in overlapped regions and addresses single-pass treatment of curved surfaces
- Calculation of three dimensional finite-element stress to analyze the stresses in near-surface regions, with particular emphasis on the transition between the martensite and underlying pearlite.
- Exploration of laser glazing methods that produce as-glazed surfaces comparable to as-produced rail.
- Theoretical analysis of the deformation behavior of rapid-solidification microstructures.
- Examination of the methodology for incorporating laser glazing equipment on rail maintenance cars.

Acknowledgement

The authors acknowledge the support of the Office of FreedomCAR and Vehicles Technologies within the U.S. DOE Office of Energy Efficiency and Renewable Energy. We are indebted to Dr. Sidney Diamond for his support of this project, in particular, for his enthusiastic support of the underlying science involved in this technology.

The authors also express their gratitude to the research staff at the Centre for Surface Transportation Technology within the National Research Council – Canada. We are indebted to Mike Krzyzanowski, Philip Marsh, Ron Koopman, Tom Davies, and Kevin Sawley for the full-scale rig tests performed in Ottawa and analysis of the data.

References

1) Energy Data Book: Edition 23; S. C. Davis and S. W. Diegel, ORNL 6970; October, 2003
2) Railroad and Locomotive Technology Roadmap; F. Stodolsky, ANL/ESD/02-6; December 2002
3) Railroad and Locomotive Technology Roadmap; F. Stodolsky, ANL/ESD/02-6, December 2002; Figure 7, courtesy of R. P. Reiff, TTCI, Pueblo, CO
4) Nuvonyx Inc.; 3753 Pennridge Dr., Bridgeton MO. 63044; St. Louis Office 314-209-7755; point-of-contact, John Haake
5) "Mitigation of Subsurface Crack Propagation in Railroad Rails by Laser Surface Modification;" R. J. DiMelfi, P. G. Sanders, B. Hunter, J. A. Eastman, K.J. Sawley, K. H. Leong, and J. M. Kramer, Surf. & Coatings Technol.; 106; (1998), 3-43
6) "Correlation between Solidification Parameters and Weld Microstructures," S. A. David and J. M. Vitek, Inter-Mater. Rev. 34 (1989), 213-245
7) "Rapid Solidification," R. Mehrabian, Inter-Mater Rev. 27 (1982), 185-208
8) "Laser Glazing, Saud Aldajah, Powerpoint presentation, DOE Vehicle Systems Program Review, Argonne National Laboratory, June, 2002
9) Transportation Technology Center, Inc. (TTCI) website; http://www.aar.com/ttci/index.htm
10) Center for Surface Transportation Technology (CSTT) website; http://cstt-ctts.nrc-cnrc.gc.ca/en/facilities/facilities07.html
11) John Haake, NuVonyx, email Haake to Fenske, Feb 3, 2004

12) Argonne National Laboratory – Evaluation of Friction Forces on Laser-Glazed Rails, CSTT-RVC-LR-012, final report from CNRC on Ottawa tests, April, 2004.

13) Principles of Tribology, edited by J. Halling, MacMillan Education, Ltd., ISBN 0-333-2486-1, 1978

14) "The Mechanical Properties of the Nanocrystalline Layer on the Surface of Railway Tracks," W. Lojkowski, Y. Millman, S. I. Chugunova, I. V. Goncharova, M. Djahanbakhsh, G. Burkle, and H. J. Fecht, Mater. Sci. and Eng. A, 303, (2001), 209-215

15) "Prevention of RCF Damage in Curved Track Through Development of the INFRA-STAR Two-Material Rail," E. J. M. Hiensch, F. J. Franklin, J. C. O. Nielsen, J. W. Ringsberg, G. J. Weeda, A. Kapoor, and B. L. Josefson, Fatigue Fract. Eng. Mater. Struct. 26, (2003), 1007-1017

16) Duroc website - www.duroc.com

APPENDIX A – CNRC WBB Rim

Figures A1 and A2 show a photograph and a schematic representation of a cross section (respectively) of the 63-in.-diameter rim segment used on the Ottawa WBB test rig. The photograph in Fig. A1 shows only one of the rim segments that make up the full 360-degree rim.

Figure A1. - Photograph of rim segment of WBB rig at Ottawa

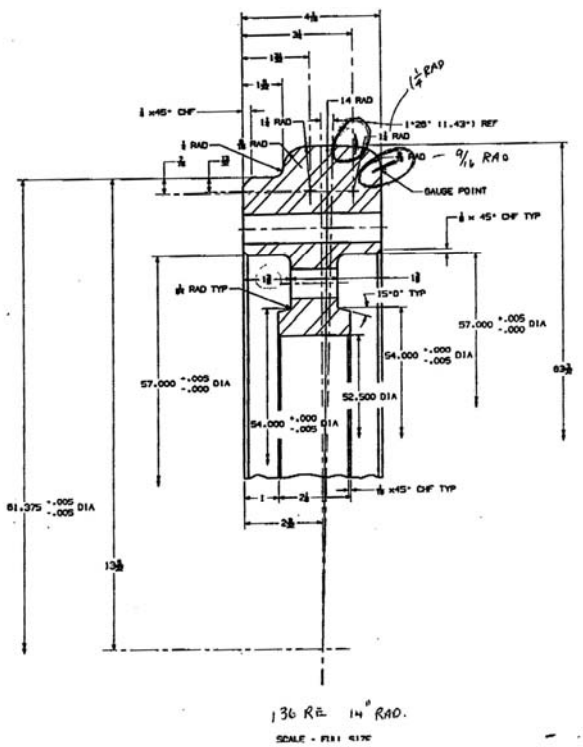

Figure A2. Schematic representation of WBBS rim, contact between wheel flange and rim occurs at 'gauge point'

APPENDIX B – CNRC WBB TEST FACILITY

The WBB facility is a large 'dual' twin-roller test rig as shown in Fig. B1. The bottom rollers simulate the rail while the top rollers are wheel sets prototypical of those used in industry. One of the wheel sets used at the WBB facility is instrumented to continuously measure the forces and moments at the wheel/rail contact.

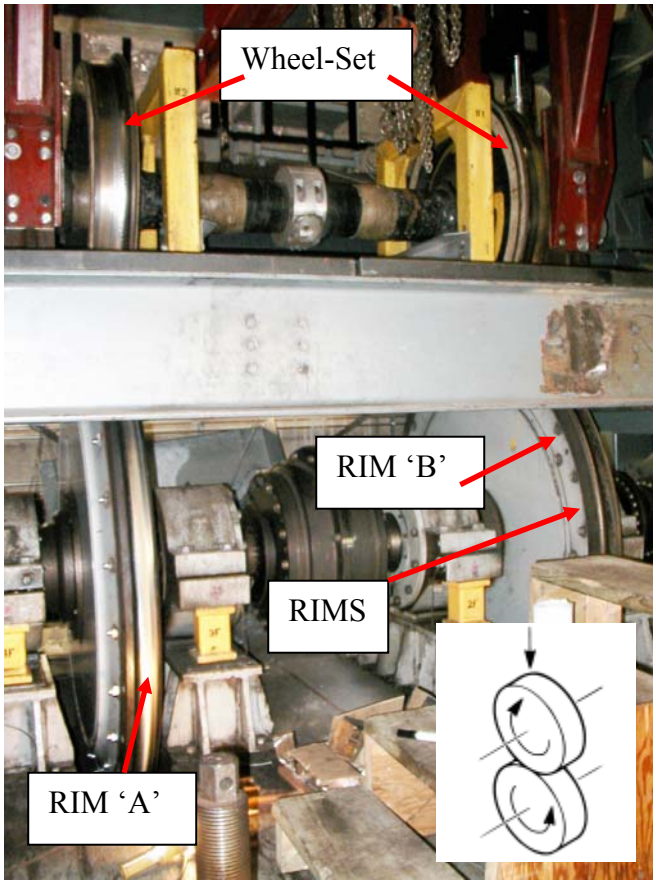

Figure B1. CNRC Wheel, Bearing, and Brake (WBB) Test Facility

Figure B2 shows a schematic representation of the wheel sets and bottom rim. Two sets of force data are recorded during the tests. The first set of force measurements ('wbb') is

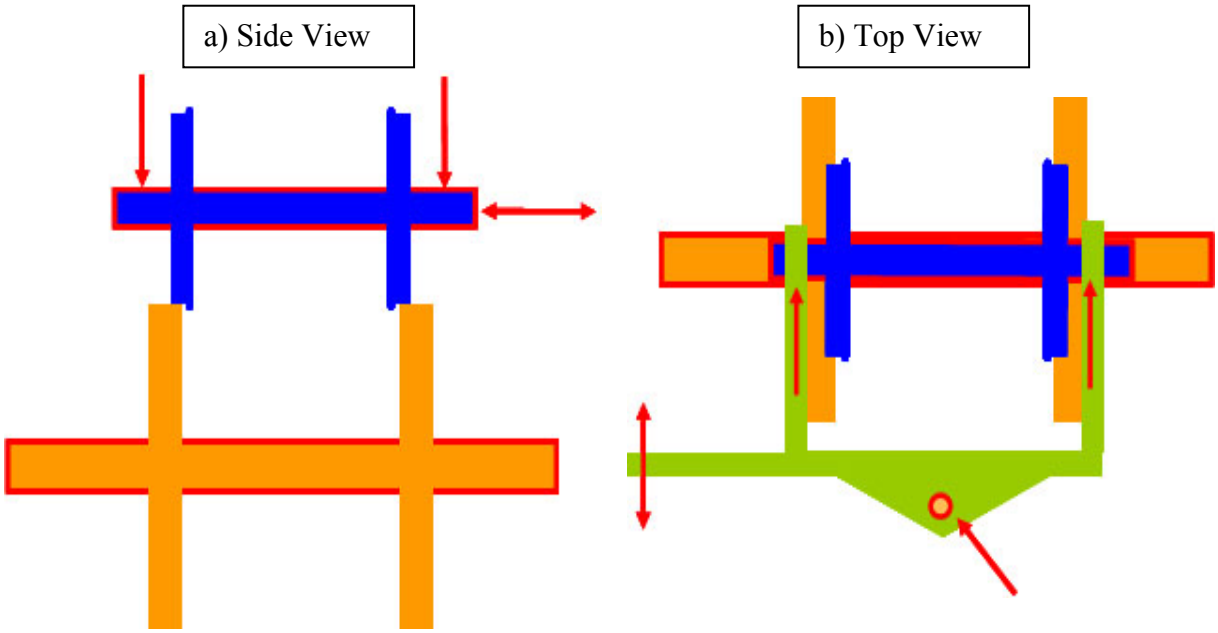

Figure B2. Schematic representation of wheel sets and bottom rim as arranged in the WBB facility: (a) Side and b) Top views of the WBB Facility

obtained from force transducers mounted on the frame of the WBB facility. The red arrows in Figs. B2 a and b show the general location of the forces. The forces measured from the WBB frame include vertical forces applied to each wheel of the top wheel set, the lateral force applied to the top wheel set, and the longitudinal forces that occur when the top wheel set is 'yawed.' The 'yaw' is introduced by rotating the top wheel set on a bearing (shown in Fig B2b).

In addition to the WBB forces, the IWS is also equipped to measure a second set of forces ('iws') on each wheel of the top wheel set. These forces, illustrated in Fig. B3, include the vertical, lateral, and longitudinal forces on each wheel. The IWS was used

during the initial set of runs (Runs 1a - 1d, see Table 1) and the final runs (5a – 5c) to provide precise measurements of the vertical, lateral, and longitudinal forces on each

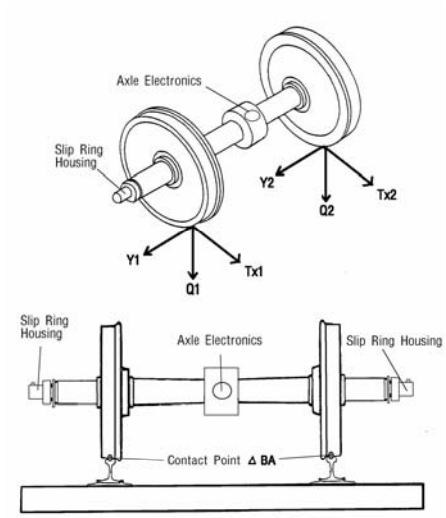

Figure B3: Forces recorded on the instrumented wheel set - IWS

wheel of the top wheel set. During these runs, data were collected at 0.005-s intervals (200 Hz) (e.g., every 1.8^{o} of rotation). This sensitivity was sufficient to discriminate between the glazed segment and the nonglazed segment, and thus provide data on the friction coefficient on each segment.

During Runs 2, 3, and 4, the instrumented wheel set was removed and replaced with a standard (less-valuable) wheel set that could endure the 'damage' incurred during the heavy-loading phase of the tests. During the latter runs, data were acquired at a much slower rate (1-Hz intervals).

APPENDIX C – FORCE MEASUREMENTS

Force measurements recorded from the WBB system of transducers include the following:

- Vertical Force Wheel 1
- Vertical Force Wheel 2
- Lateral Force
- Yaw Force Wheel 1
- Yaw Force Wheel 2

Forces recorded with the IWS system included:

- Vertical Force Wheel 1
- Vertical Force Wheel 2
- Lateral Force
- Yaw Force Wheel 1
- Yaw Force Wheel 2

+

- IWS Vertical Force Wheel 1
- IWS Vertical Force Wheel 2
- IWS Lateral Force Wheel 1
- IWS Lateral Force Wheel 2
- IWS Longitudinal Force Wheel 1
- IWS Longitudinal Force Wheel 2

$$\text{Friction Coeff} = \frac{[\,(\text{Lat.})^2 + (\text{Long.})^2\,]^{1/2}}{\text{Vertical Force}}$$

During Runs 1a-d, the friction coefficient was determined from the IWS vertical force on **Wheel 2**, IWS lateral force on **Wheel 2**, and the IWS longitudinal force on **Wheel 2**. For Runs 5a-c, the IWS was flipped around, and the friction coefficient was determined from the IWS vertical force on **Wheel 1**, the IWS lateral force on **Wheel 1**, and the IWS longitudinal force on **Wheel 1**.

A more rigid calculation of the friction coefficient would include the lateral forces, to determine the 'normal' force in the denominator; however, the magnitude of the lateral force (e.g., 4,000 lb for Run 5c) is small when compared with the vertical force (e.g., 40,000 lb for Run 5c), and, thus, including the lateral force in the denominator does not significantly affect the friction coefficient.

APPENDIX D – FRICTION DATA

Run 1a: A film of oil was observed on the rims after Run 1a, and the friction data were not analyzed because the oil film influenced the friction data. The oil film was removed and the test was repeated (Run 1b)

Run 1b: Run 1b lasted approximately 10 minutes at a speed of 6 mph, and a load of roughly 10,000 lb. Initially, Run 1b was running tangentially (low or zero yaw). At t = 100s, yaw was applied and ramped up until approximately 480 s, and then held constant. Figures D1-D3 show the vertical, lateral, and longitudinal forces on the IWS, respectively for Run 1b. The vertical force was a control parameter. The load was ramped up from near zero to 8000 lb, then up to roughly 10,000 lb at t = 60 seconds. At approximately t = 100 s, (Fig. D2), yaw was initiated and continuously increased until approximately t = 480 s.

Figure D4 shows the calculated friction coefficient as a function of time during the entire run. The oscillations in the friction coefficient as the glazed and nonglazed segments rotate under the IWS are hard to discern at the scale shown in Fig. D4. To observe the changes, it is necessary to examine the forces on a shorter time scale, i.e., at 10-s increments. To illustrate this, Figure D5 shows a series of graphs that reveal the vertical load (as measured from the WBB transducer), and the vertical, lateral, and longitudinal loads measured with the IWS transducers. At a speed of 6 mph, the bottom rim (63 in. in diameter) turned one revolution every 1.9 s, and, thus, the 10-s increment represents data

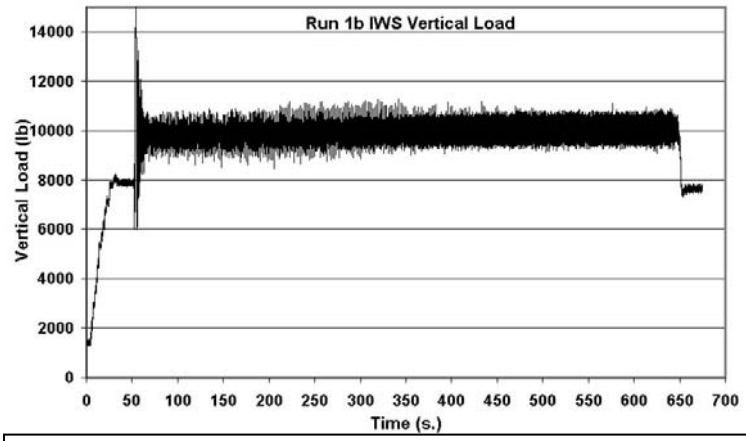

Figure D1. IWS vertical force history during Run 1b.

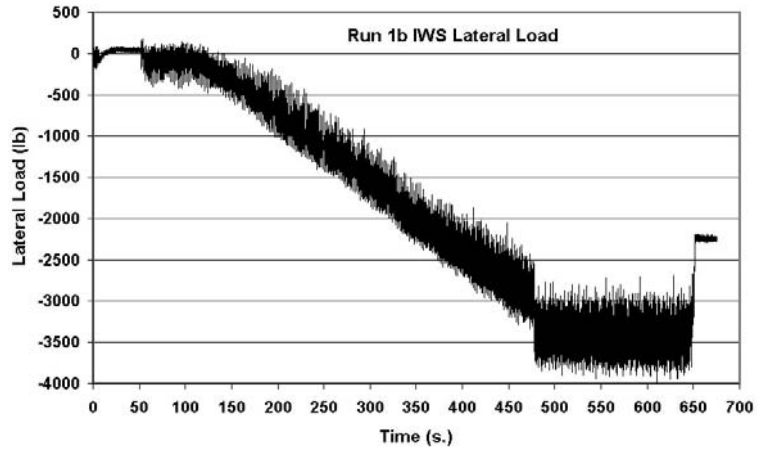

Figure D2. IWS lateral force history during Run 1b.

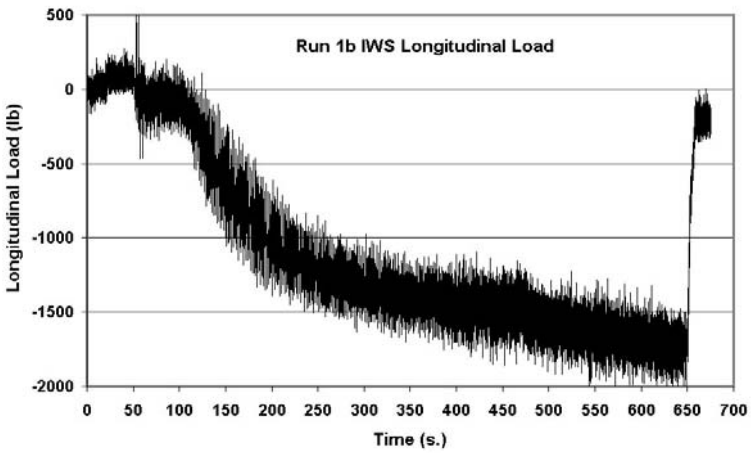

Figure D3. IWS longitudinal force history during Run 1b

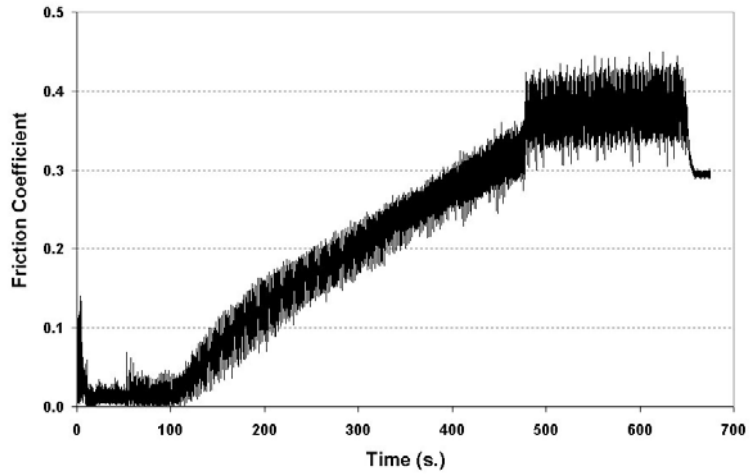

Figure D4. Friction during Run 1b

collected at approximately every 5 revolutions. The difference between the absolute values of the WBB and IWS vertical load measurements is due to the location of the WBB load transducer; the WBB forces do not incorporate the forces due to the weight of

the IWS wheel set, whereas the IWS measurements inherently include these measurements.

As seen in Fig. D5, the WBB vertical load measurements show two distinct trends/levels of loading during each revolution: a relatively smooth load trace while contact occurs between the nonglazed rim segment and the IWS wheel, and a rougher load trace when the glazed rim segment comes in contact with the IWS wheel. The rougher trace for the glazed rim segment is due to the rougher finish the glazed track; the glazed rim was not refinished to remove the surface roughness introduced by the glazing process. (This is an important feature to note; in practice, a smoother finish [consistent with current rail] will be required. How to accomplish this, either by refining the glazing protocol, or refinishing, must be addressed. The surface finish will also affect the friction and the stresses in near-surface regions.)

Figure D6 shows the friction coefficient obtained by using the IWS data for the vertical, lateral, and longitudinal loads and the equation in Appendix C. As seen in Fig. D6, the friction coefficient for the glazed rim segment was lower than that for the nonglazed rim segment.

Friction (and WBB vertical load curves) for other time intervals during Run 1b are shown in Figs. D7-D14.

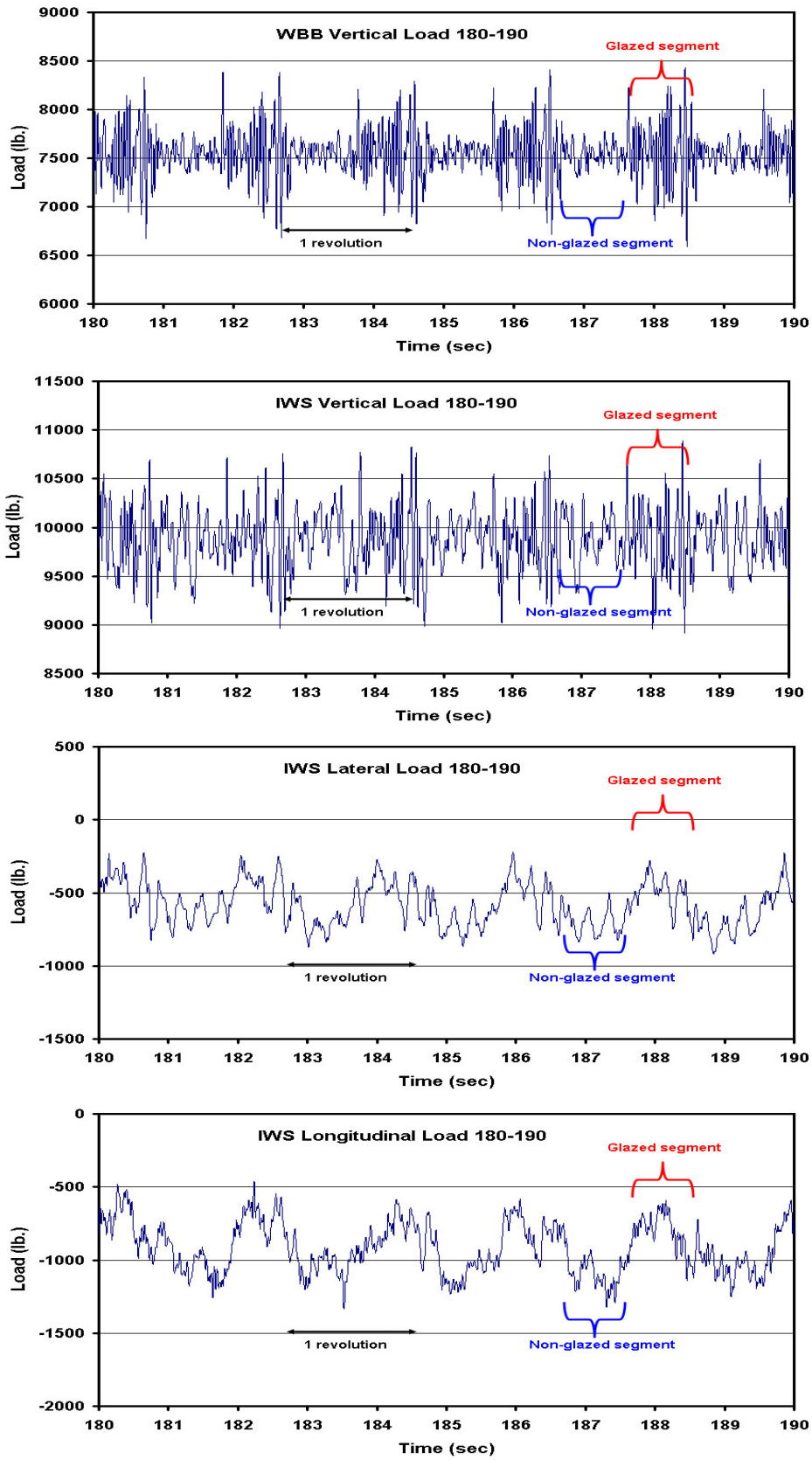

Figure D5. Transducer forces during Run 1b (180-190 s)

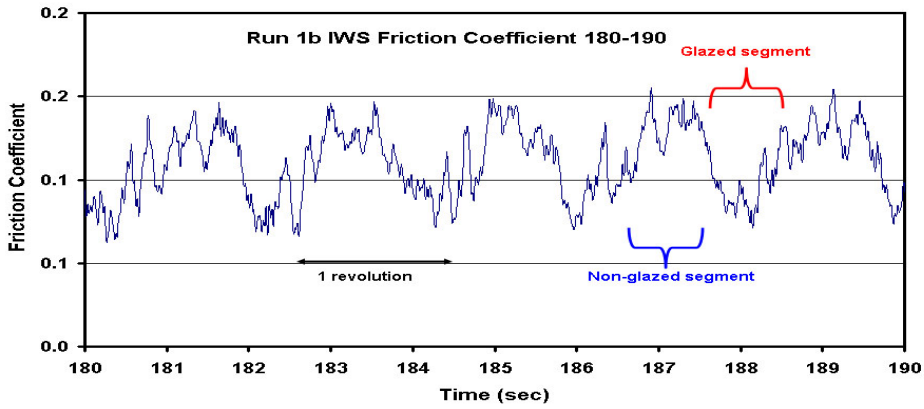

Figure D6. Friction coefficient for Run 1b (180-190 s)

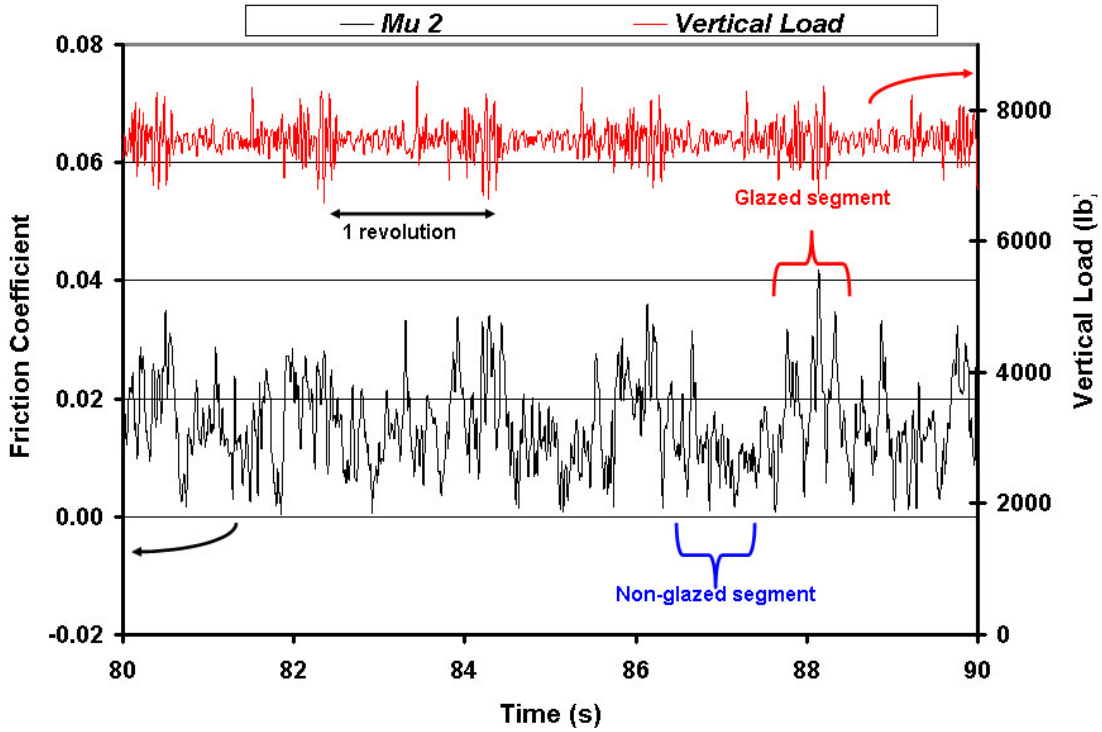

Figure D7. Friction and WBB vertical load between 80 and 90 s during Run 1b

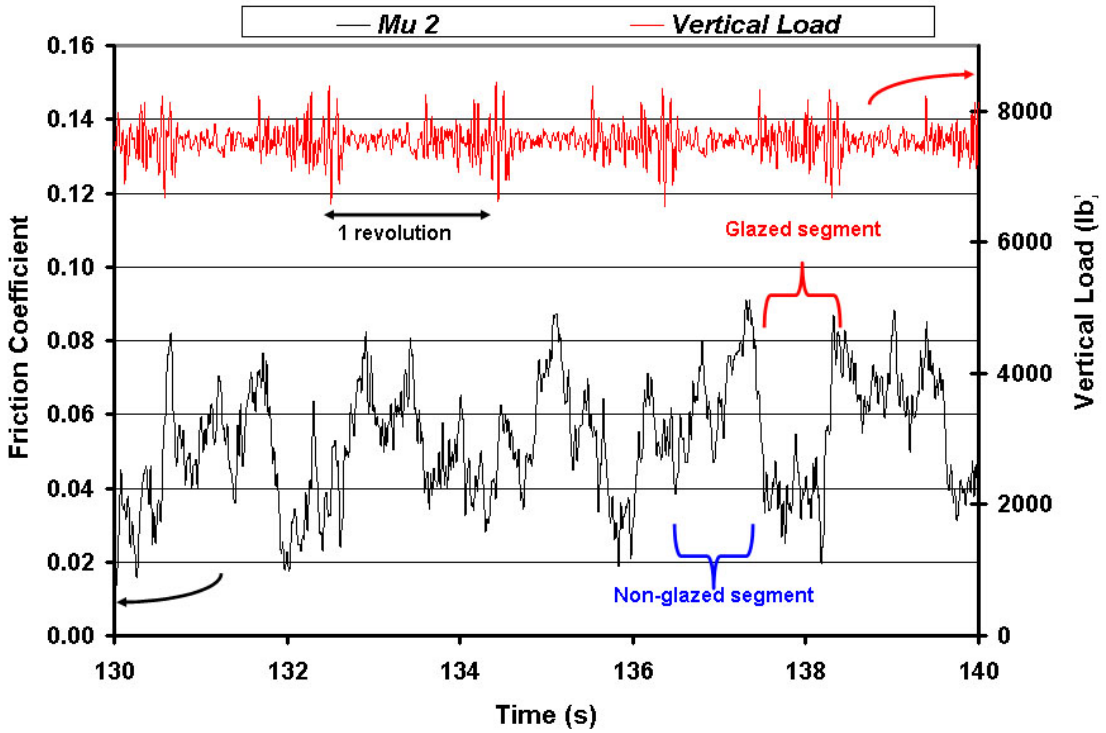

Figure D8. Friction and WBB vertical load between 130 and 140 s during Run 1b

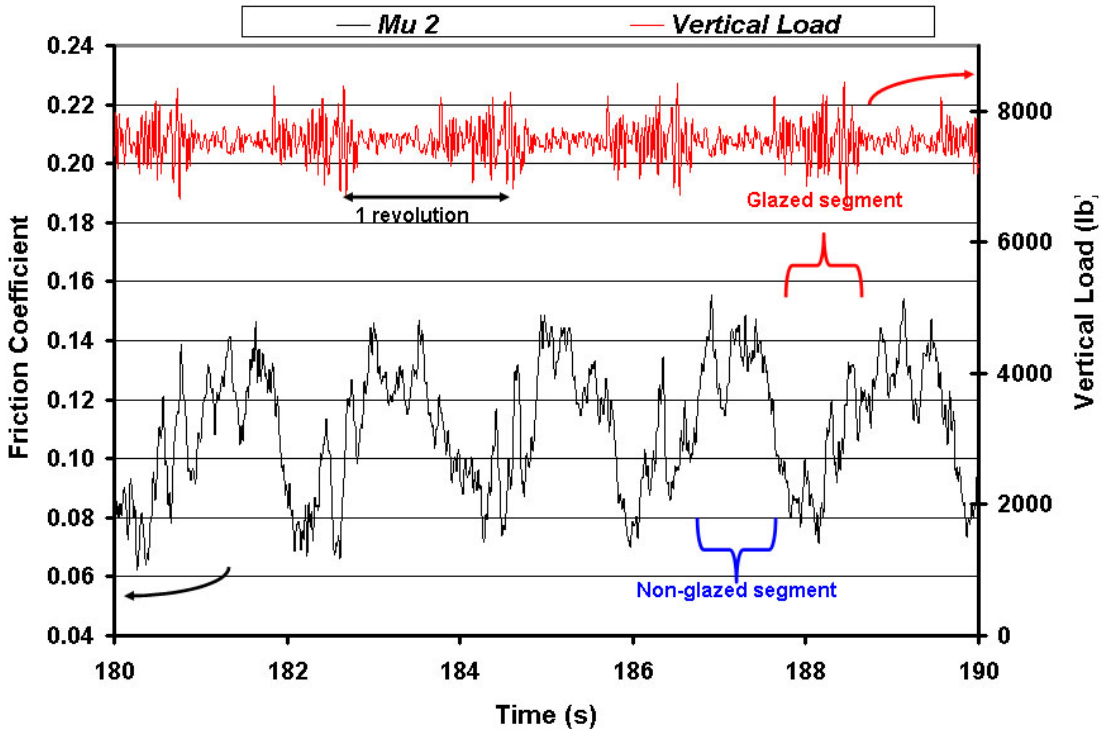

Figure D9. Friction and WBB vertical load between 180 and 190 s during Run 1b

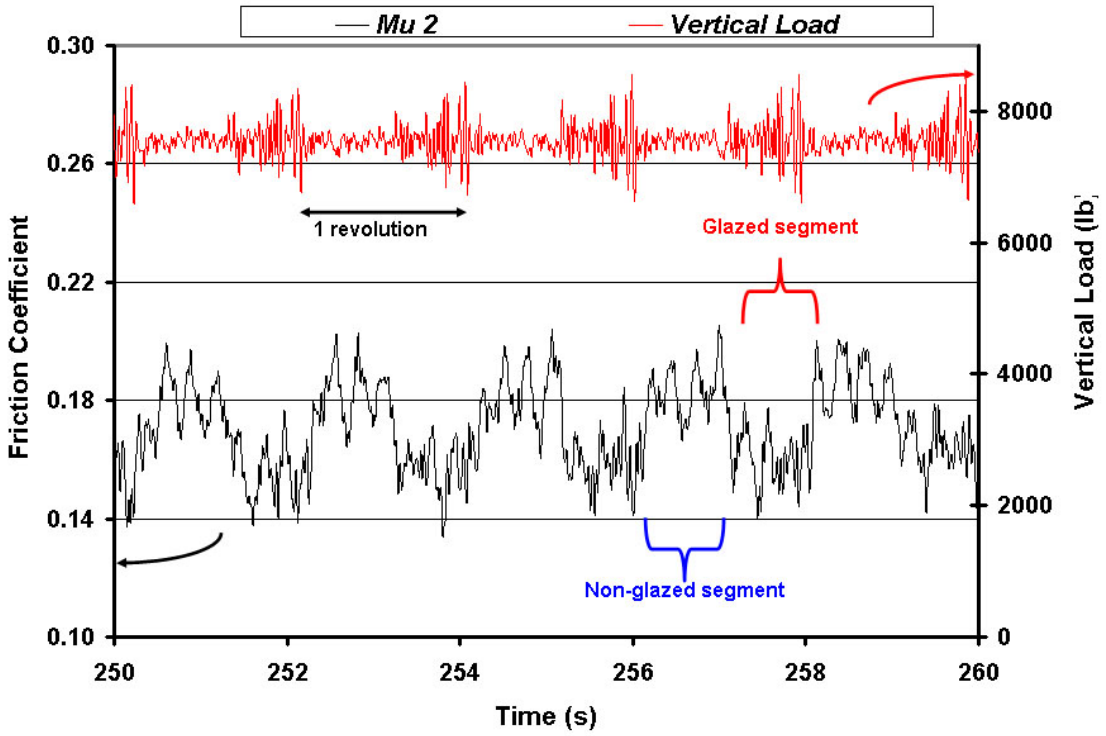

Figure D10. Friction and WBB vertical load between 250 and 260 s during run 1b

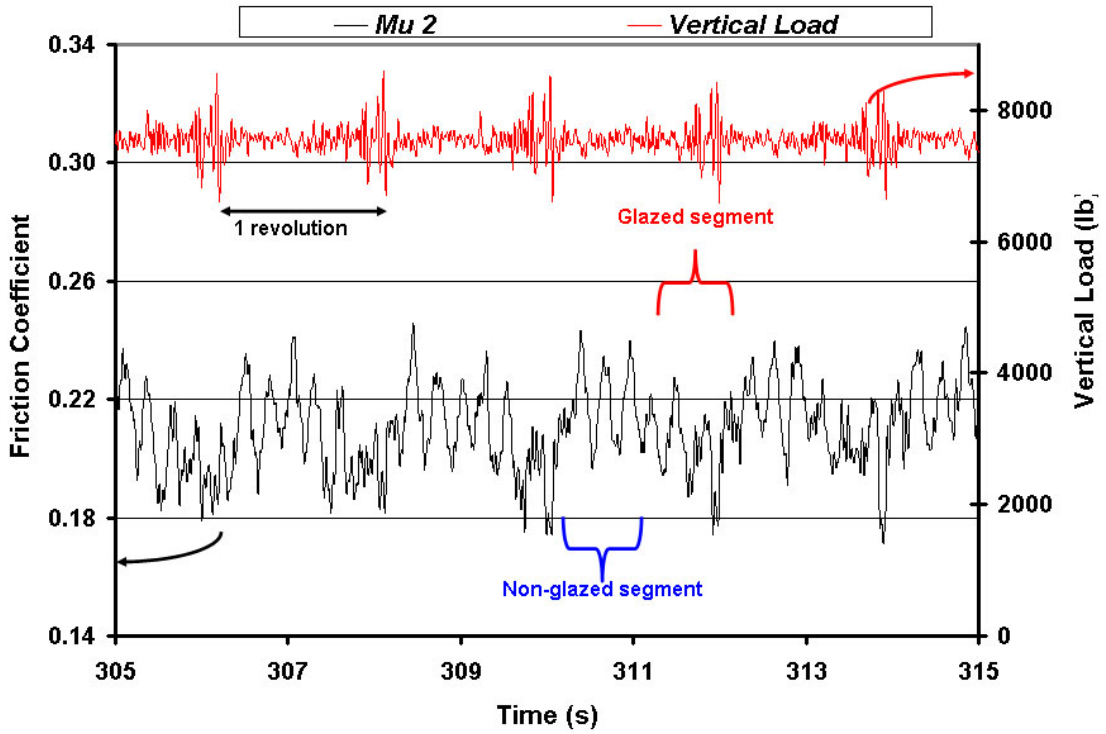

Figure D11. Friction and WBB vertical load between 305 and 315 s during Run 1b.

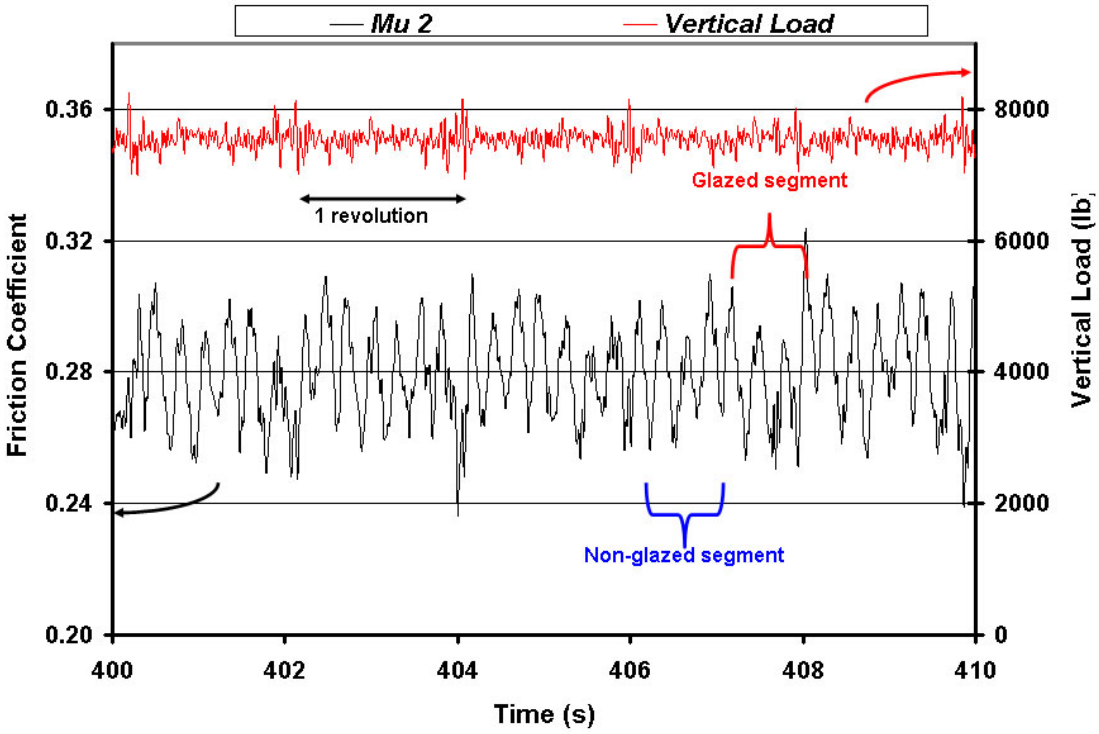

Figure D12. Friction and WBB vertical load between 400 and 410 s during Run 1b

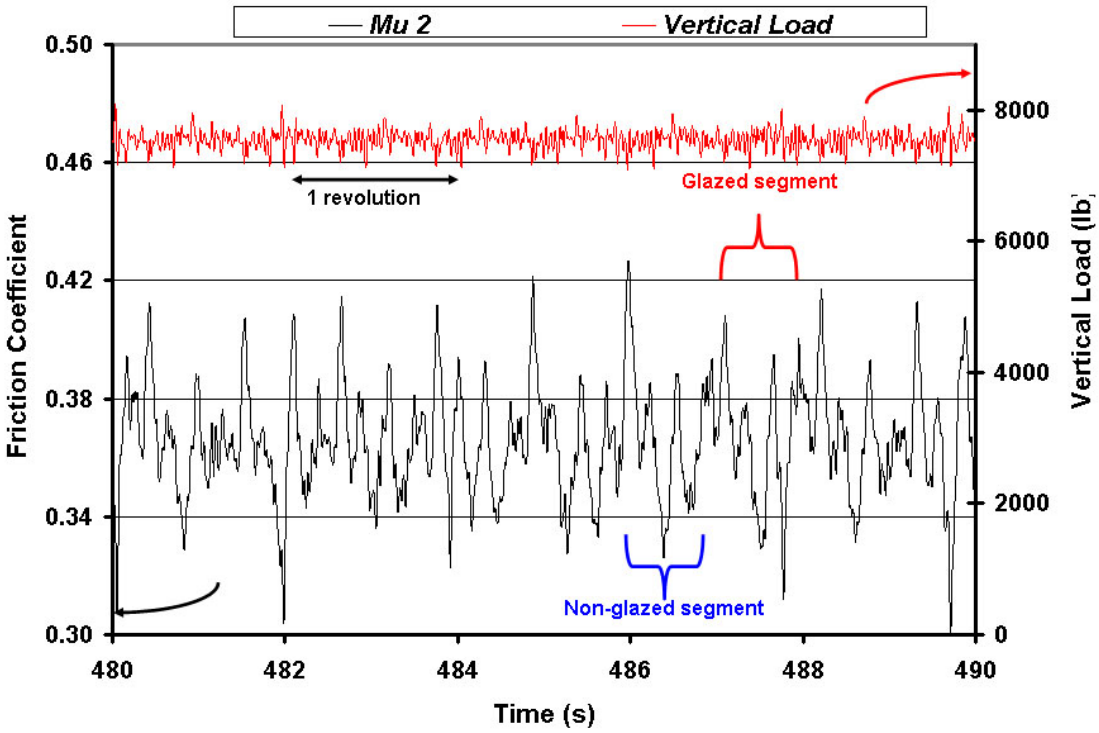

Figure D13. Friction and WBB vertical load between 480 and 490 s during Run 1b

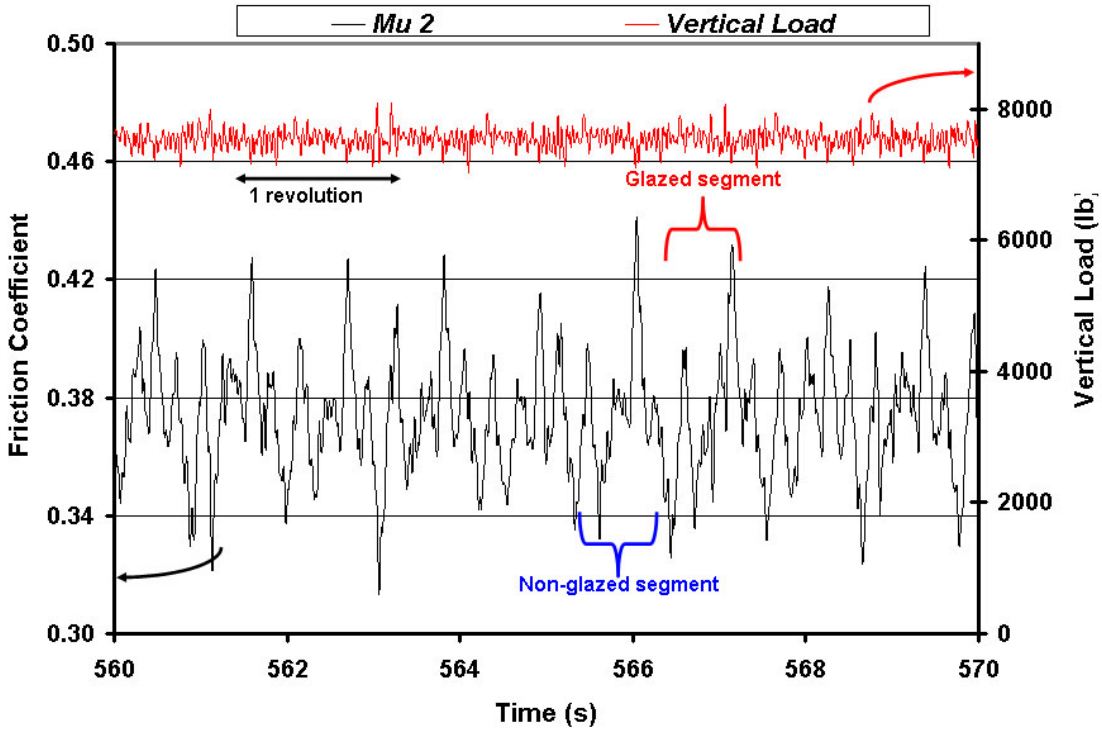

Figure D14. Friction and WBB vertical load between 560 and 570 s during Run 1b

Runs 2, 3, and 4. These runs were long(er)-term tests than Runs 1 a-d. The IWS wheel set was removed and replaced with a conventional noninstrumented wheel set, and, thus, friction data were not recorded.

Runs 5a-c. After the long-term tests (runs 2-4) during which the rim accumulated approximately 1 MGT exposure, the IWS was reinstalled, and a series of runs was performed to measure the friction response. Data from Runs (5a-c) are shown in Figs. D15-D27

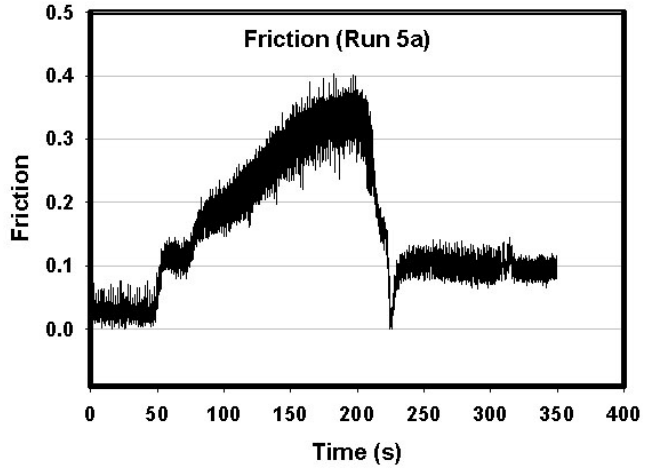

Figure D15. Friction during Run 5a.

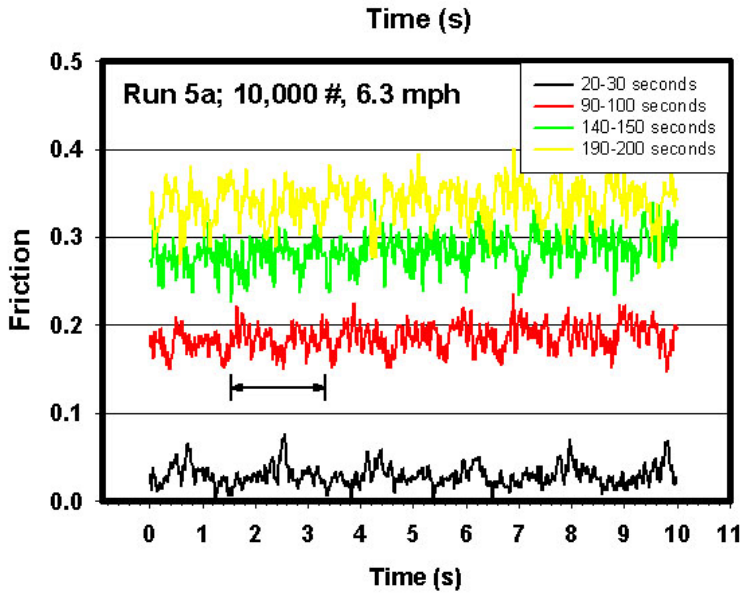

Figure D16. Friction during various 10-second intervals of Run 5a

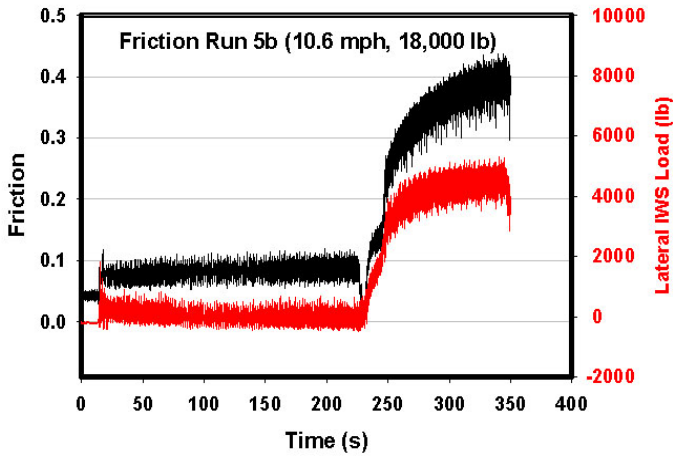

Figure D17. Friction during Run 5a.

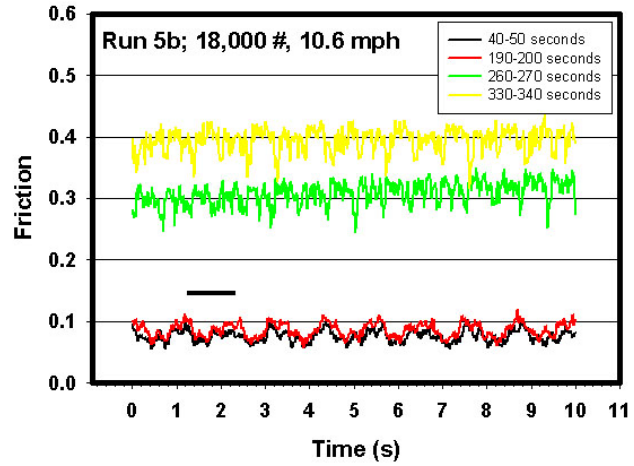

Figure D18. Friction during various 10-second intervals of Run 5b

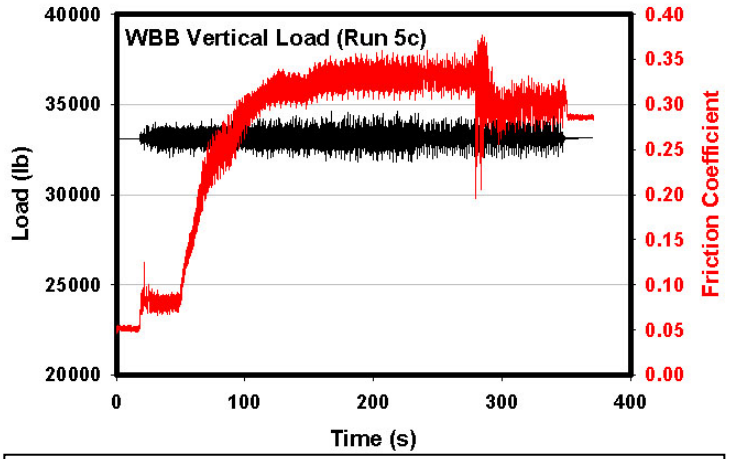

Figure D19. Friction and IWS lateral load during Run 5c

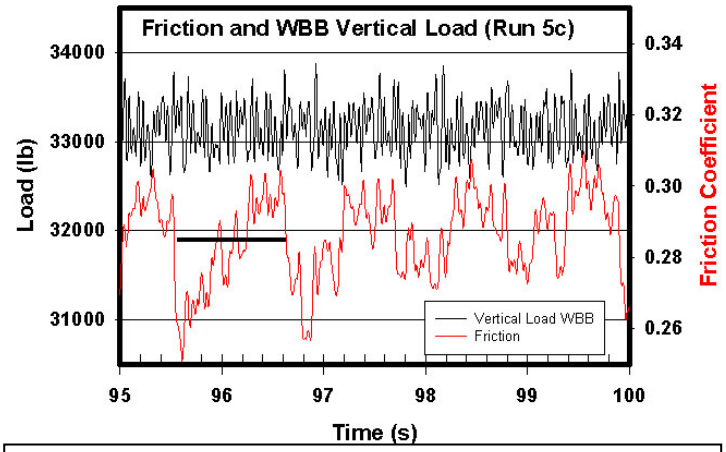

Figure D20. Load and friction during Run 5c (95-100 s)

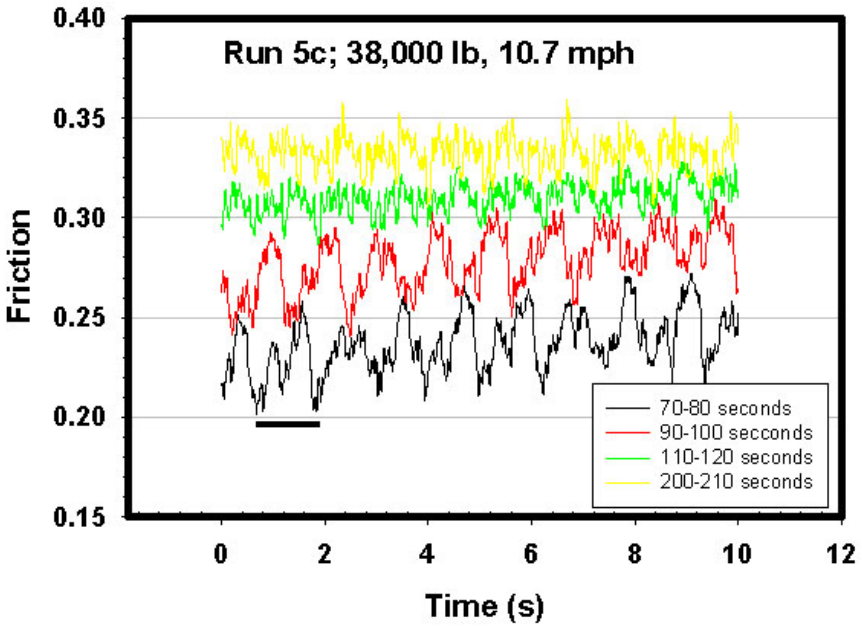

Figure D21. Friction during various 10-s intervals of Run 5c

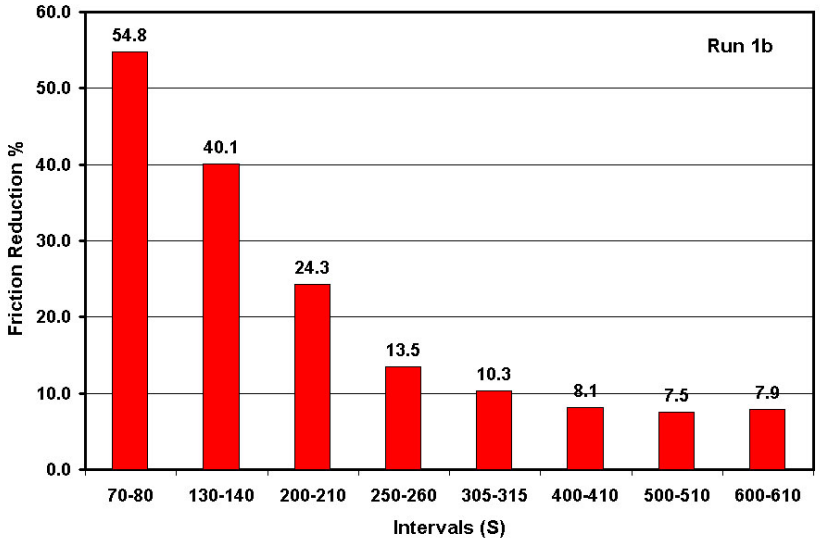

Figure D22. Friction reduction on glazed rim (normalized to unglazed rim segment) for Run 1b

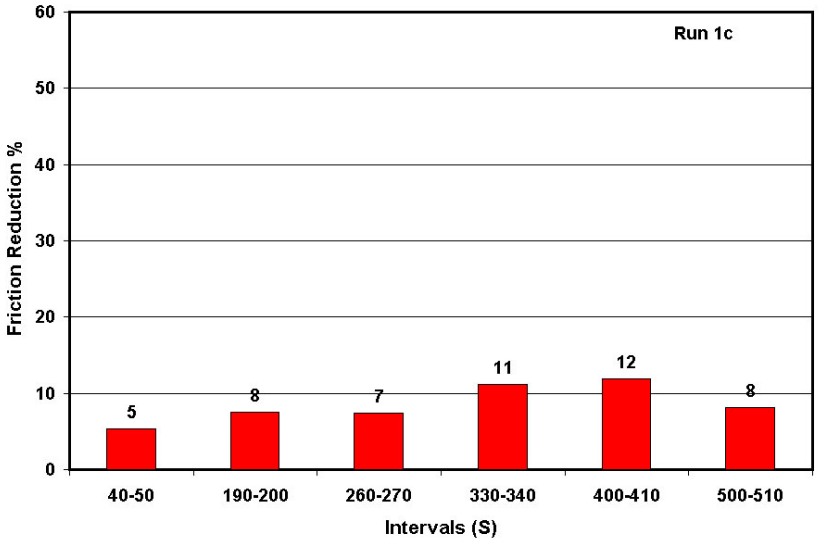

Figure D23. Friction reduction on glazed rim (normalized to unglazed rim segment) for Run 1c

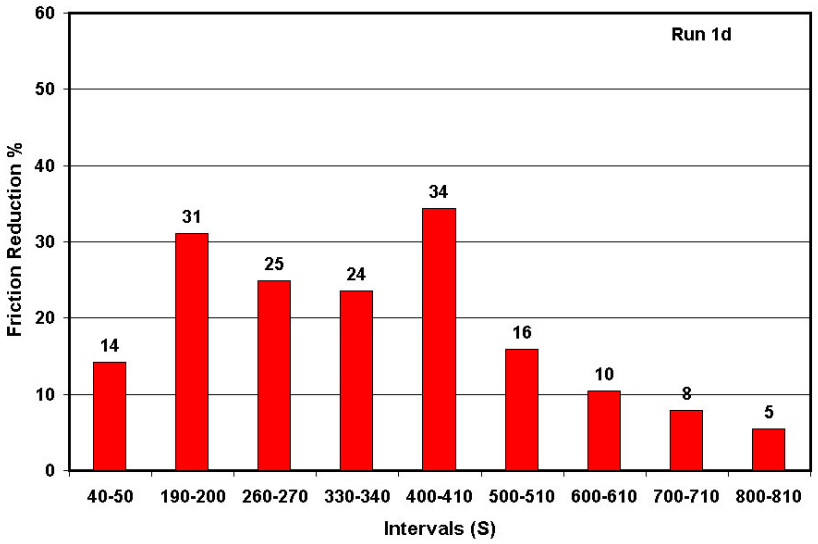

Figure D24. Friction reduction on glazed rim (normalized to unglazed rim segment) for Run 1d

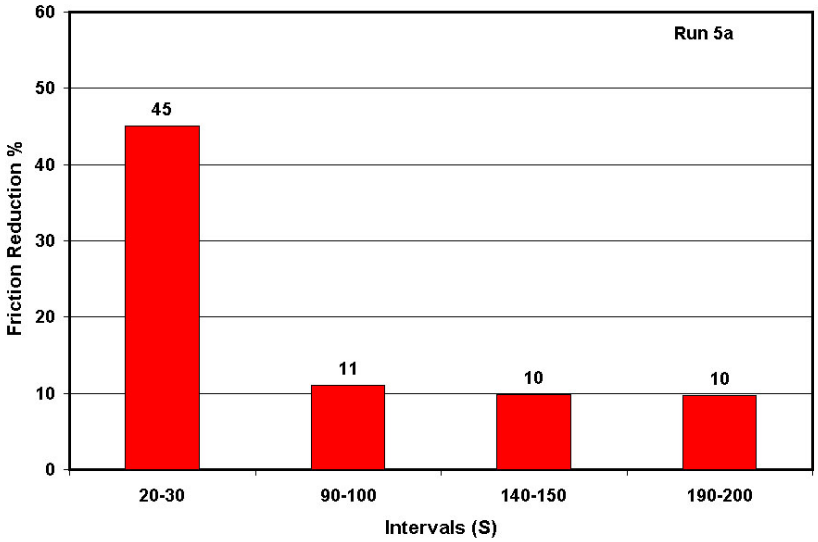

Figure D25. Friction reduction on glazed rim (normalized to unglazed rim segment) for Run 5a.

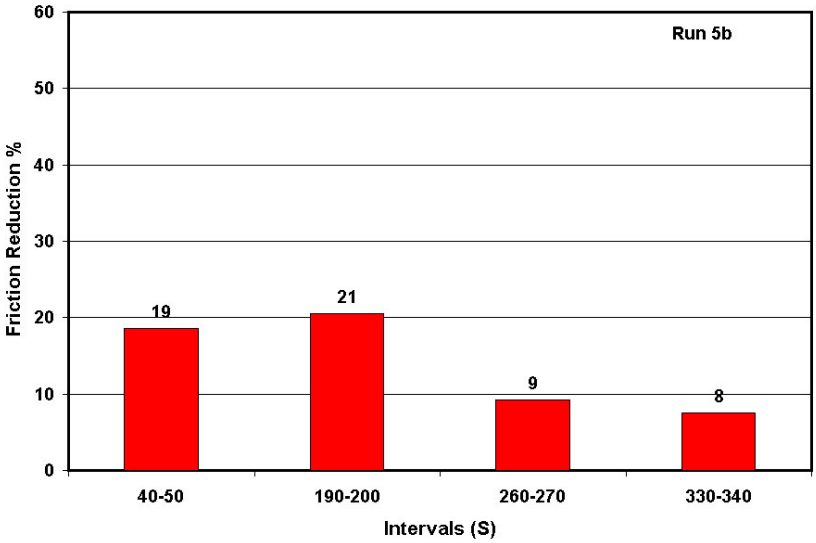

Figure D26. Friction reduction on glazed rim (normalized to unglazed rim segment) for Run 5b

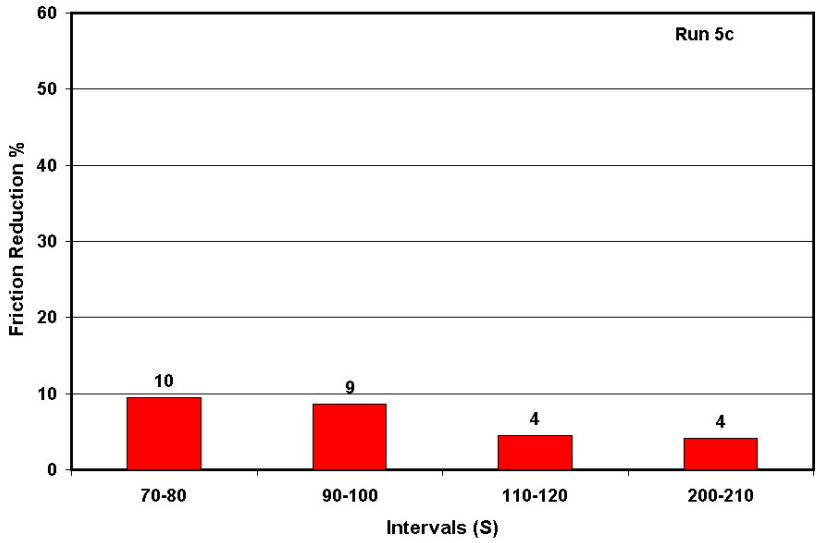

Figure D27. Friction reduction on glazed rim (normalized to unglazed rim segment) for Run 5c

Run 5a was a repeat of Run 1b (approximately 6 mph and 10,000 lb load). The results are shown in Figs. D15 and D16 (D16 shows 10-second intervals). Some cyclic behavior is evident, but not as pronounced as in Run 1b.

Run 5b was performed with a heavier load (18,000 lb) and a higher speed (10 mph). The results are shown in Figs. D17 and D18. A definite cyclic behavior is observed during the beginning of the run, when the load was applied but before yaw was applied (see Fig D18). When yaw was applied, the friction increased, and the cyclic behavior was not as pronounced, nevertheless, some degree of cyclic response was observed.

Run 5c was performed at a higher load (38,000 lb) at a speed of approximately 10.6 mph. The friction data are shown in Figs. D19 and 21.

APPENDIX E – MAGNAFLUX IMAGES (After run 4d)

After Run 4, the glazed rim was treated with magnafluxing compound to facilitate imaging of the glazed rim to determine if microcracks developed. The results of the magnafluxing imaging are shown in Figs. E1 and E2. Images E1a and b were taken at the ends of the rims, in particular, at the very ends where the glazing track ends. Image E2 was obtained further in from the ends of the glazed segment at a location approximately 6-10 in. from one end. Image E2 actually is very close to location '3' (see Appendix F), where replicas were taken at various times during the test sequences.

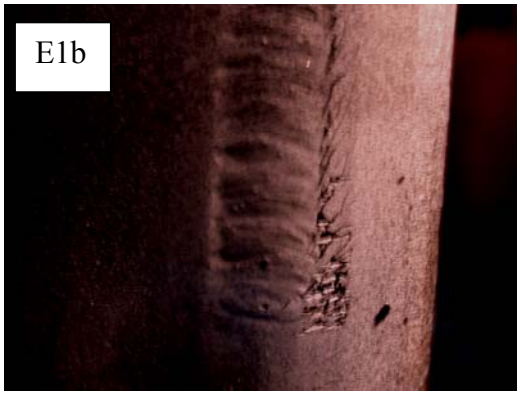

Figure E1a & b. Magnaflux images of glazed track ends after Runs 1-4.

Microcracks are evident in Figs. E 1a and b, however, the microcracks do not appear to occur inside the glazed track, they appear to terminate at the boundary between the glazed and non-glazed region. Another feature to note is that the microcracks are located to the right of the glazed track, between the glazed track and the gauge point. No cracks were observed to the left of the glazed track. The image seen in Fig. E2 shows that microcracks are present and that a section of glazed area is missing, i.e., the material was pulled out. Analysis of the replicas from this region indicates that the pull-out region

Figure E2. Magnaflux image of glazed region near Location 3 (Appendix F)

coincided with a region that 'stuck out' from the rest of the glazed region because it was rougher. The increased stresses that would be the result of the higher peak in this region could readily account for the increased fatigue beneath this region.

Appendix F - Replica Photographs

At various times during the runs, the tests were stopped and, with the aid of microset replicating compound (http://www.microset.co.uk/media/index.html), replicas were taken at the locations designated Locations 1, 2, or 3 (Fig. F1) along the glazed rim.

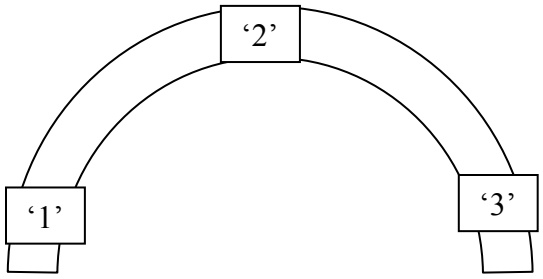

Figure F1. Locations of Microset replicas.

Replicas were taken before the start of runs 1 a-d were designated as Replicas 1-0, 2-0, and 3-0; before the start of Run 2a, as Replicas 1-1, 2-1, and 3-1 (as well as another set designated as Replicas 1-1a, 2-1a, and 3-1a); before the start of Run 3a, as Replicas 1-2, 2-2, and 3-2; and before run 5a, as Replicas 1-3, 2-3, and 3-3. After the replicas were taken, they were coated with a layer of Cr (a few 100 nm thick to enhance optical imaging of the replicas.

Figures F2, F3, and F4 show sequences of photographs obtained from the replicas for Locations 1, 2, and 3, respectively. The semitransparent rose-colored regions in these figures show the locations of the glazed track (located on the top surface of the glazed

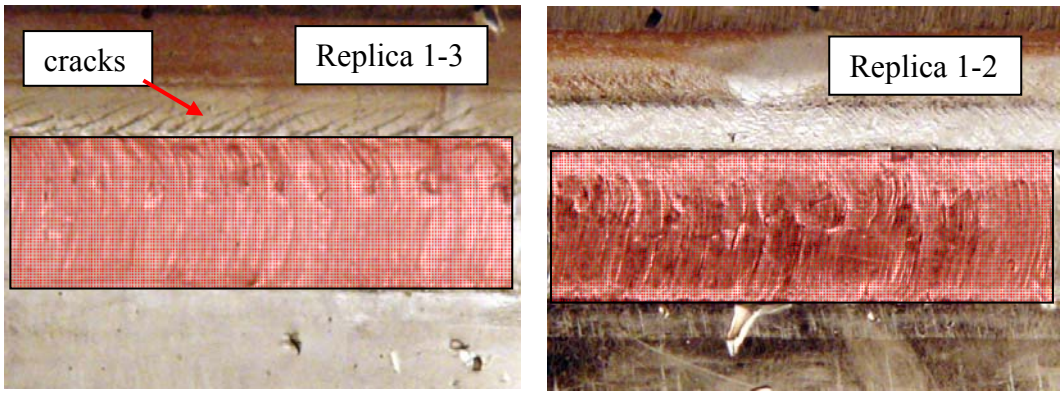

Figure F2. Photographs of replicas from Location 1

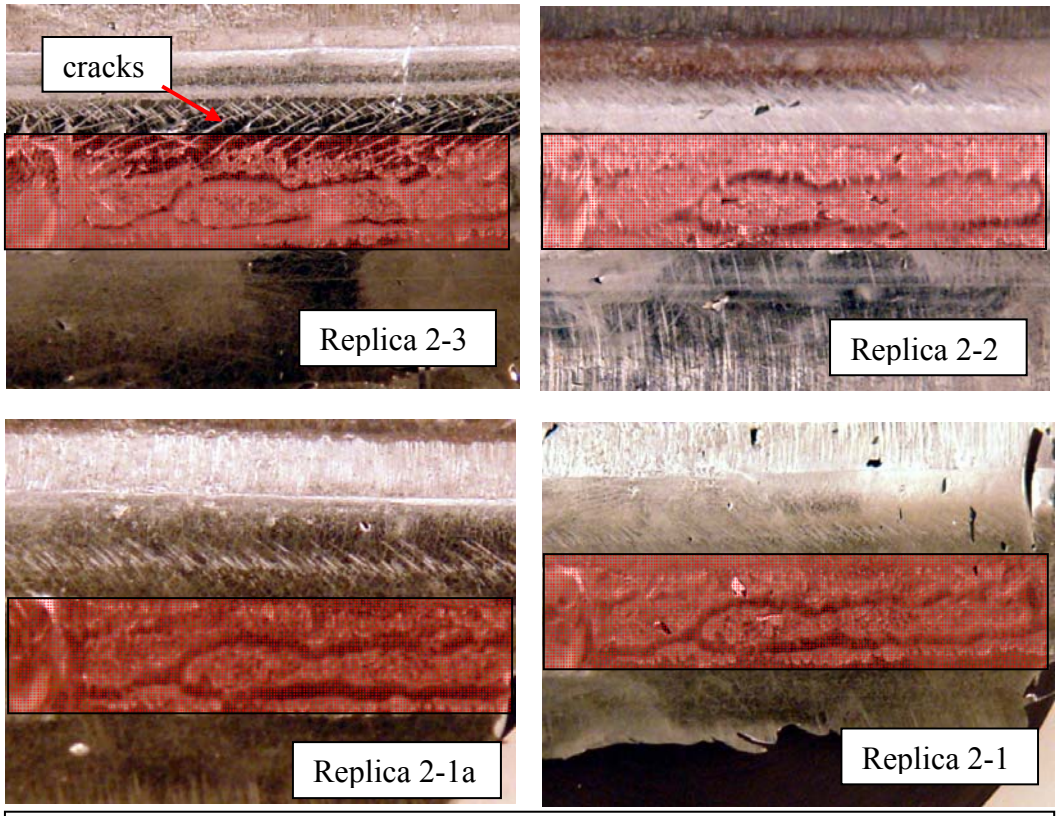

Figure F3. Photographs of replicas from Location 2

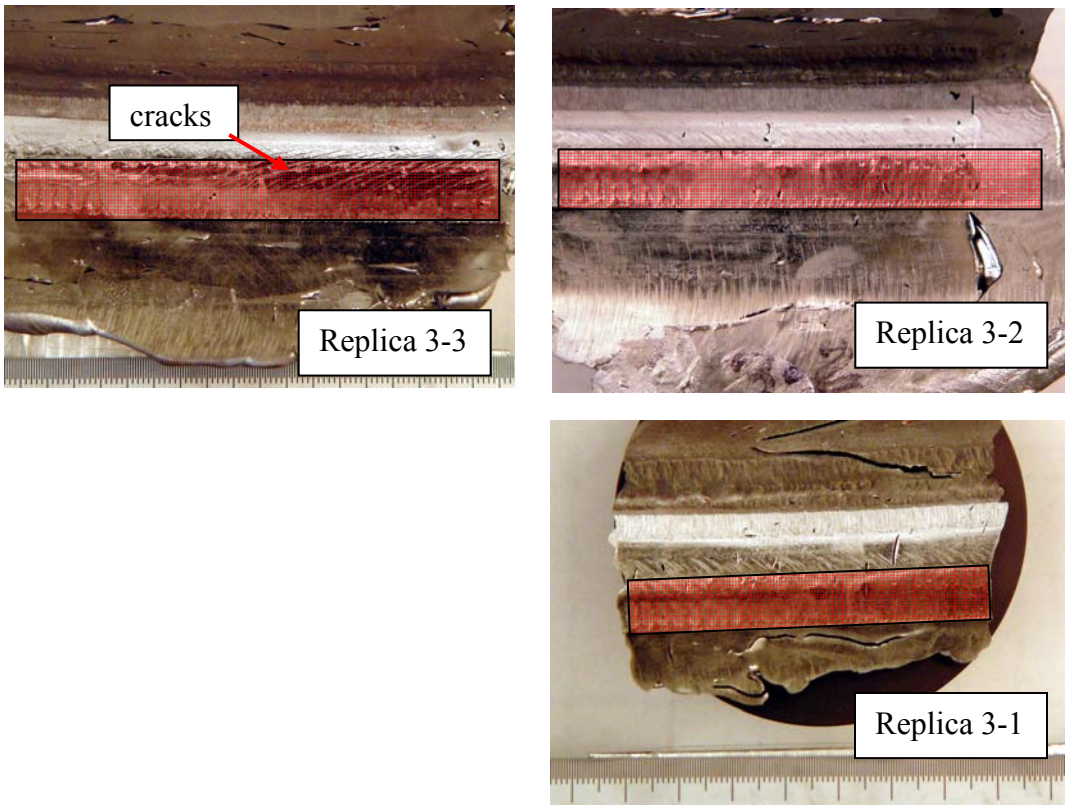

Figure F4. Photographs of replicas from Location 3

rim). The critical feature to note in these Figures is the presence of cracks just above the laser tracks for the images/replicas taken just before Run 5a (e.g., after the heavy-tonnage runs, Runs 2, 3, and 4). The cracks (corresponding to Replica 1-3 in Fig. F2, Replica 2-3 in Fig. F3, and Replica 3-3 in Fig. F4) are primarily located just above the glazed track and typically do not extend into the glazed track. The other feature to note is that the cracks do not occur below the glazed track.